On the unfolding of the energy spectrum measured by the HEAT extension at the Pierre Auger Observatory

von

Sebastian Hartmann

Masterarbeit in Physik

vorgelegt der
Fakultät für Mathematik, Informatik und Naturwissenschaften
der
RWTH Aachen University

im Dezember 2015

angefertigt am

III. Physikalischen Institut A

Erstgutachter und Betreuer
Prof. Thomas Hebbeker
III Physikalisches Institut A
RWTH Aachen

Zweitgutachter
Prof. Martin Erdmann
III Physikalisches Institut A
RWTH Aachen

Contents

1 Introduction

The Pierre Auger Observatory [1, 2], located in the Pampa in Mendoza, Argentina, combines multiple detection methods to detect high-energy cosmic rays. The main detector components consist of 1660 water-Cherenkov detectors spread over an array of 3000 km^2 on the surface and 24 standard fluorescence telescopes on the edge of the array observing the atmosphere above the surface detectors. The connection of these detection methods allow for the combination of the positive detector properties while minimizing their weaknesses.
The High Elevation Auger Telescopes (HEAT) [2] extend the standard fluorescence telescopes by three upward tilted telescopes, located near Coihueco. These telescopes lower the energy threshold due to the possibility to detect showers with little fluorescence light, which evolve closer to the telescope site in higher parts of the atmosphere.

The limited acceptance and finite resolution of every detector lead to distorted and transformed measured distributions. In order to compare the results of different experiments the measured distributions have to be unfolded.
As unfolding is an ill-posed problem, advanced methods has to be applied and regularization has to be performed.
In order to understand the influence of the detector on the data the response matrix, which connects the sought quantity to the observed one, has to be established. Therefore Monte Carlo data has to be created using CONEX [3] and the OFFLINE detector simulation framework [4] by the Pierre Auger Collaboration.

Two different methods will be applied to the data measured by HEAT.
First, a method by G. D'Agostini commonly called Bayes' Unfolding [5] is applied to the data measured by HEAT. This algorithm uses Bayes' theorem iteratively to unfold the measured spectrum. The limited number of iterations serves as a regularization.
Then, an algorithm called SVD Unfolding by A. Höcker and V. Kartvelishvili [6], which uses the Singular Value Decomposition is introduced. Regularization is performed by adding a regularization term proportional to the matrix of second finite derivatives of the distribution.

These analysis have to be performed for different interaction models and primary particle assumptions.
The resulting unfolded energy distribution can be compared to results from other experiments.

2 Cosmic Rays and the energy spectrum

In 1912 Victor Hess first discovered cosmic radiation with a balloon experiment [7]. He found, that the ionizing radiation increased at higher altitudes which got him to the conclusion that the radiation must be travelling from outer space into the atmosphere. The charged nature of the cosmic radiation was shown by Bothe and Kolhörster [8] in 1929.

In 1938 Pierre Auger performed experiments at the Jungfraujoch, Switzerland. [9] He used Geiger-Müller tubes at altitudes of 3500 meter above see level in coincidence mode, but spatial separated by more then 100 m. His observations of coincident signals led to the conclusion of extensive air showers (EAS) which are produced high up in the atmosphere by primary cosmic ray particles and develop in a cascade towards the ground.

During the following decades up to today many other experiments were designed and build to study the features, sources and many other aspects of the cosmic radiation.

The spectrum of the cosmic rays (see figure 2.1) can be described best by a power law

$$dN/dE \propto E^{-\gamma} \tag{2.1}$$

with two additional features. At energies between 10^{10} eV and $10^{15.5}$ eV the spectral index γ is roughly 2.7. At 10^{15} eV the spectrum becomes steeper and the spectral index up to energies around $10^{18.5}$ eV increases to about 3.1. In the highest energy regime above $10^{19.5}$ eV the flux is highly suppressed. [10]

The first bend in the spectrum in the PeV energy regime is called the knee, the second one at EeV energies is called the ankle (following the picture of a leg). To emphasize these features the flux is usually scaled by some power (here $E^{2.5}$) of the energy as shown in figure 2.2.
Possible explanations for the knee, the ankle and the cut-off at highest energies are presented and discussed in [11].

Extensive Air Showers

On Earth it is not possible to detect cosmic rays directly. When entering the atmosphere they interact with molecules in the atmosphere and secondary particles are produced. These secondary particles again may collide with further nuclei in the atmosphere and a cascade, the so called extensive air shower (EAS), will be triggered. Until the energy loss through ionisation becomes dominant, the cascade continues to develop up to its maximum. The particles continue travelling towards the ground without creating new particles. In the end, mainly electrons any muons hit the ground. There are different types of possible cascades which are sketched in figure 2.3. An

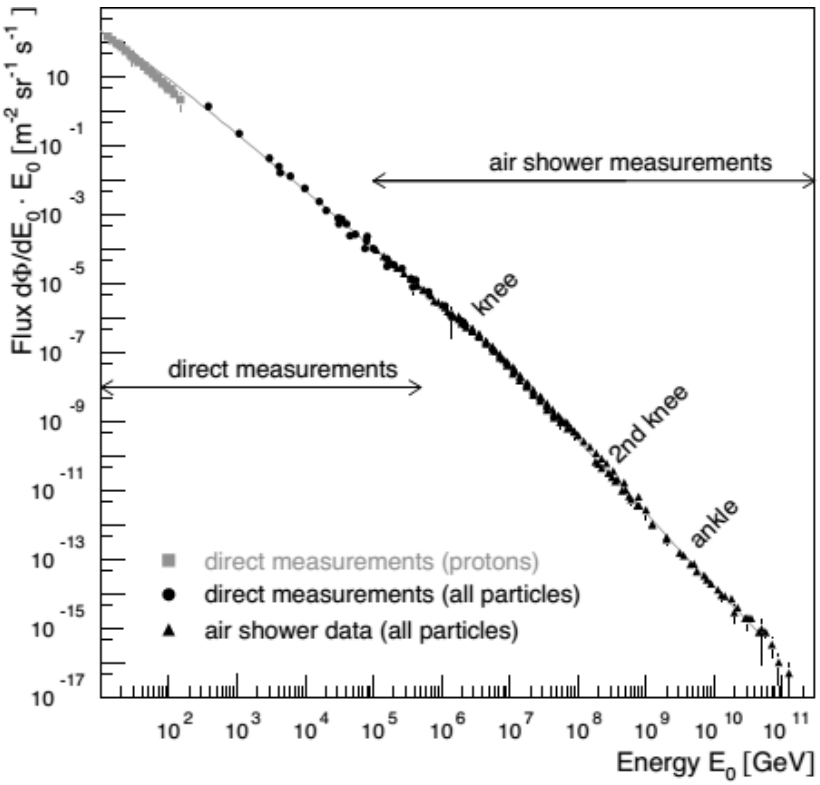

Figure 2.1: All-particle energy spectrum of cosmic rays as measured directly with detectors above the atmosphere and with air shower detectors. At low energies, the flux of primary protons is shown. From [11].

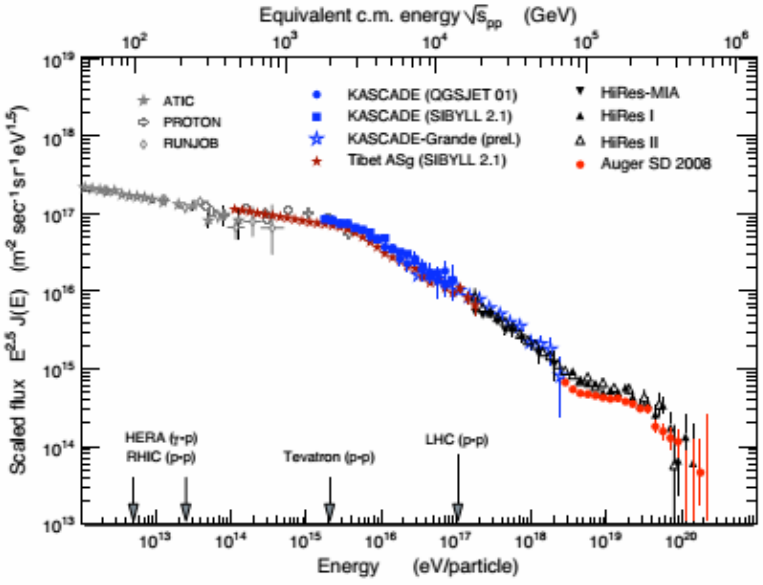

Figure 2.2: All-particle cosmic-ray energy spectrum scaled by $E^{2.5}$. From [11]. For origin of data also see [11].

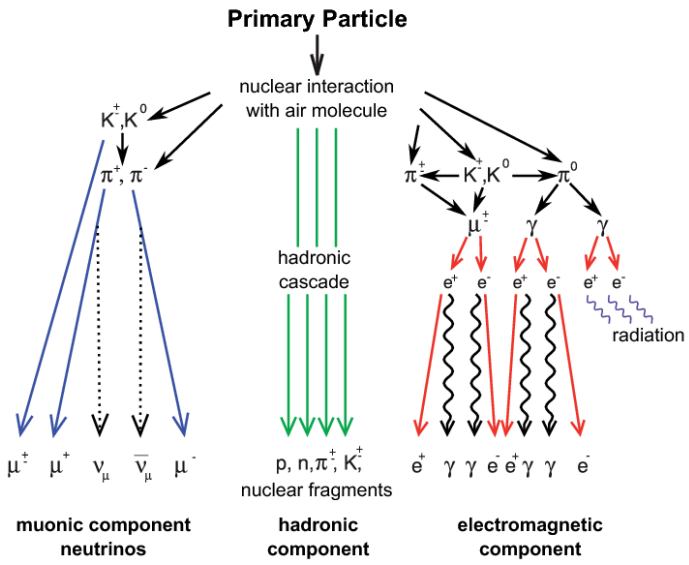

Figure 2.3: Schematic view of an extensive air shower (EAS). From [12].

electromagnetic cascade which consists of photons, electrons and positrons and a hadronic cascade which is created when a hadronic particle enters the atmosphere. A hadronic cascade typically contains also an electromagnetic part triggered by secondary electromagnetic particles produced in the early hadronic cascade.

Heitler model

A simplified but reasonably accurate model to describe the stochastic development of extensive air showers was introduced by W. Heitler in 1954 [13].

Initial particles penetrate the atmosphere and interact with the molecules within the radiation length λ_0 producing two secondary particles. Electrons (and positrons) interact mainly in terms of bremsstrahlung and radiate a high energy photon, whereas high energy photons decay in the process of pair production and produce an electron-positron pair. The number of particles can be calculated as

$$N(X) = 2^{\frac{X}{ln2 \cdot \lambda_0}} \tag{2.2}$$

with X being the slant atmospheric depth:

$$X(h, \theta) = \frac{1}{\cos\theta} \int_h^\infty dh' \rho(h'). \tag{2.3}$$

The atmospheric depth integrates the local matter density $\rho(h')$ a particle travelled through in the atmosphere and is therefore given in g/cm^2.

As the energy of the interacting or decaying particle is transferred equally into two new particles, every particle carries a fraction of the energy E_0 of the primary particle:

$$E = \frac{E_0}{N(X)} \tag{2.4}$$

Pair production and bremsstrahlung only occur at high energies. When the particle energy drops below a critical energy E_c the development of the cascade stops and the maximum is reached. The number of particles at the maximum of the shower is linked linearly to the initial energy:

$$N(X_{max}) = \frac{E_0}{E_c} \tag{2.5}$$

The slant depth of the shower maximum is therefore proportional to the logarithm of the initial energy:

$$X_{max} = \lambda \cdot \frac{ln(E_0/E_c)}{ln(2)} \tag{2.6}$$

A more advanced model to describe the electromagnetic component of the extensive air showers is parametrized by the Gaisser-Hillas function [14]:

$$N(X) = N_{max} = \left(\frac{X - X_0}{X_{max} - X_0}\right)^{(X_{max}-X)/\lambda} exp\left(\frac{X_{max} - X}{\lambda}\right) \tag{2.7}$$

While the Gaisser-Hillas function describes the longitudinal development of the shower, Nishimura, Kamata and Greisen [15, 16] introduced a function to parametrize the lateral particle distribution.

This distribution is mainly influenced by Coulomb scattering. The large area that is covered can be described by the inverse proportionality of the scattering angle with respect to the particle energy. Therefore electrons scatter further from the shower axis away as the shower develops.

3 The Pierre Auger Observatory

In the following chapter the Pierre Auger Observatory will be introduced. This will be mainly a summary of [1] and [17]. For more information on the Surface Detector see [18], for details about the Fluorescence Detector see [19]. Other parts of the Pierre Auger Observatory that are not covered in detail in this thesis are the Auger Engineering Radio Array (AERA) [20] and the Auger Muons and Infill for the Ground Array (AMIGA) [21].

3.1 Surface Detectors

The surface detector (SD) of the Pierre Auger Observatory consists of 1660 water-Cherenkov tanks spread over an area of 3000 km^2. They are positioned in a hexagonal grid with a spacing of 1500 meters. A smaller area within the regular area is instrumented with a maximum spacing of 750 meters. This subarray is called Infill. [22] A picture of a surface detector tank is shown in 3.1. Each tank has a diameter of 3.6 m and is filled with 12000 l of pure water. Particles passing through the detector at velocities higher than the speed of light in water produce Cherenkov-light which is detected by three twelve inch photomultiplier tubes (PMTs) inside the tank. Power supply for each station is provided by a battery and solar panel kit. In order to communicate via wireless network with the central data acquisition system (CDAS) each station has a communication antenna and a GPS clock for local timing information.
The SD reaches its full efficiency at energies above $10^{18.5}$ eV. An important feature of the surface detector is its duty cycle of nearly 100%.

3.2 Fluorescence Detectors

In addition to the surface detectors there are 24 fluorescence detectors (FD) located at four buildings around the SD instrumented area. At each of the four sites Coihueco, Los Leones, Loma Amarilla and Los Morados there are six telescopes observing the sky above the SD tanks. Additionally there are three more telescopes at Coihueco as part of the High Elevation Auger Telescope extension which will be described in section 3.3. The telescopes follow a modified Schmidt camera design with an additional corrector ring. Fig. 3.3 shows the setup of one telescope.

Each telescope has a field of view of $30° \times 30°$ which adds up to a total field of view of 180° in azimuth and 0° to 30° in elevation for each telescope site. To detect the fluorescence light, that is emitted by previously excite atmospheric nitrogen molecules a PMT camera is used. To protect the optical instruments from dust and climate

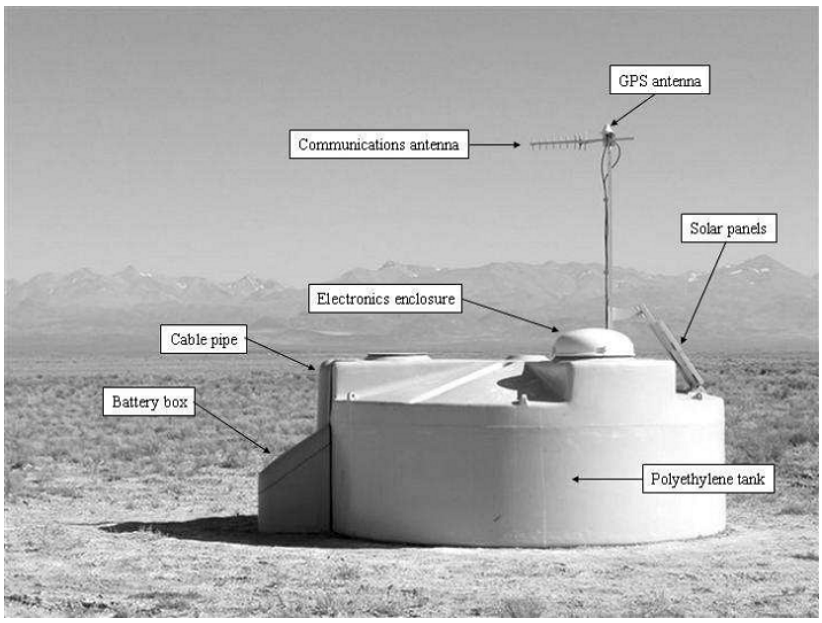

Figure 3.1: A schematic view of a surface detector station in the field, showing its main components. From [18].

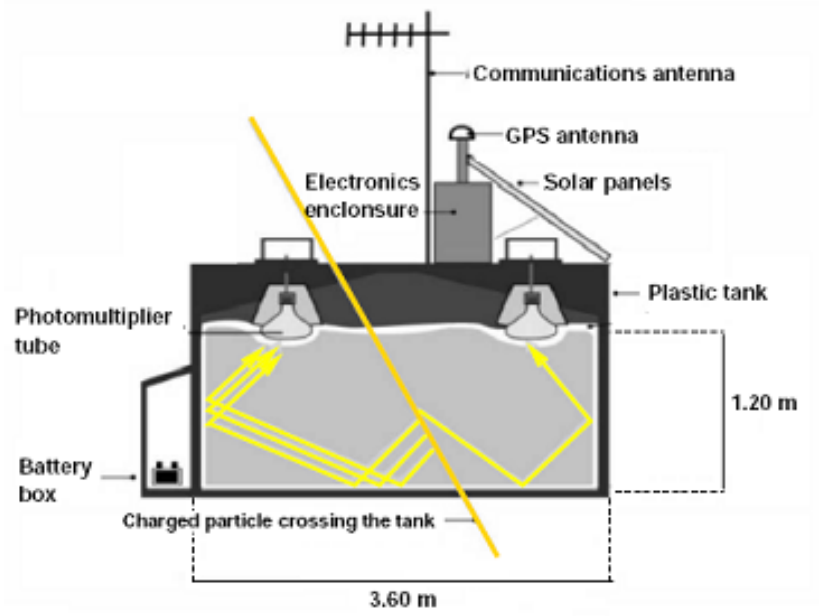

Figure 3.2: A schematic view of the inside of a surface detector station. From [23].

influences and to provide stable measurement conditions the telescopes are build into houses. The wall the telescope is facing is covered by an UV-passing filter window followed, with respect to the way of light, by a corrector ring. The filter is designed to reduce the background signal outside the wavelength range from 310 nm to 390 nm. To compensate for coma aberration as well as to reduce spherical aberration the corrector

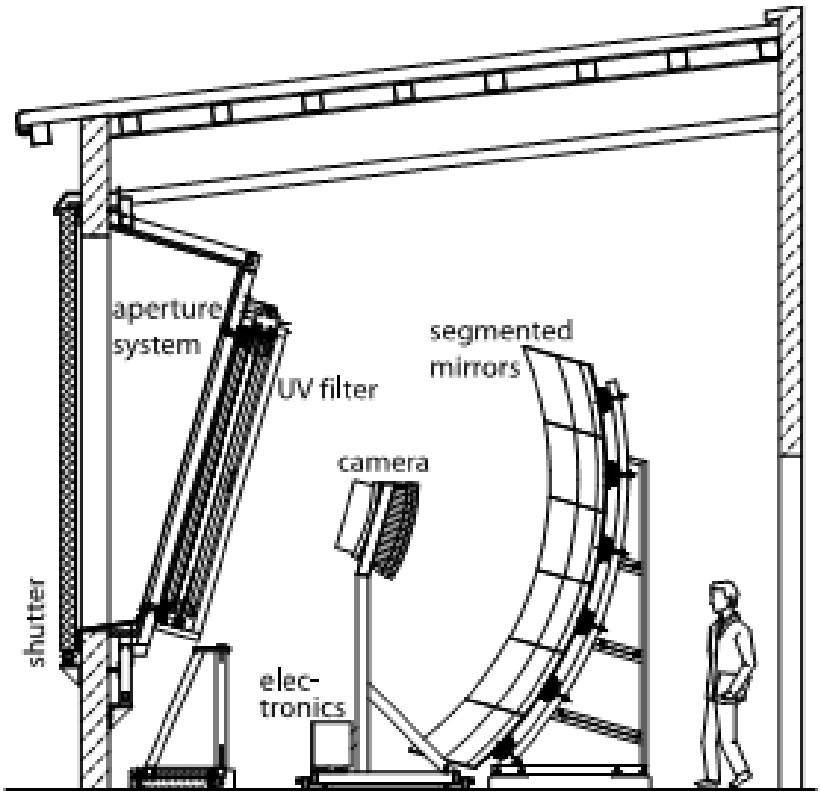

Figure 3.3: Schematic view of a fluorescence telescope of the Pierre Auger Observatory. From [19].

Figure 3.4: Fundamental types of pattern regarded as straight track segments. From [19].

ring with an inner radius of 850 mm and an outer radius of 1100 mm is used. A 13 m^2 mirror focuses the light onto the PMT camera which consists of 440 pixels with a viewing angle of 1.5° each.

Three different trigger levels are used before the event data is read out. The first level trigger applies after the signal exceeds an certain threshold during a defined time. Secondly, the pattern of the signal is checked and the second level trigger is accepted if at least four signal pixels match a straight line, as shown in figure 3.4. Finally, the third level trigger is supposed to reject noise events, like events triggered by lightning, direct muon impacts or randomly triggered pixels. The total event rate for one telescope site yield 0.012 Hz. [1]

Due to the high sensitivity of the PMT camera the FD telescopes are only operating during moonless and clear nights, which leads to a much lower duty cycle of only about 13% [19] compared to the SD.

When charged particles travel through the atmosphere they are capable of exciting nitrogen molecules. When relaxing, these molecules produce fluorescence light, mainly at wavelength of 300 to 400 nm, which is emitted isotropically. Therefore the shower can be detected from any given angle. It can be shown [24], that

$$\frac{dN_\gamma}{dX} = \frac{dE_{dep}^{tot}}{dX} \int Y(\lambda, P, T, u) \cdot \tau_{atm}(\lambda, X) \cdot \epsilon_{FD}(\lambda) d\lambda \tag{3.1}$$

which yields a connection between the deposited energy E_{dep}^{tot} and the number of photons N which can be detected. Further components of the formula are the fluorescence light yield Y (depending on wavelength λ, atmospheric pressure P, temperature T and humidity u), the transmission of the atmosphere τ_{atm} and the fluorescence detector efficiency ϵ_{FD}.

The calibration of the fluorescence telescopes is performed by using a drum shaped light source which is mounted in front of each telescope (see fig. 3.5). The drum contains a calibrated, pulsed UV LED that emits light at about 365 nm.

Hybrid event reconstruction The geometrical reconstruction of the shower profile starts with the so called shower detector plane (SDP). This plane is defined by the path the shower takes and the detector which detects it.
To reconstruct the shower axis within the SDP the timing information from the individual pixels are used. The time t_i at which the i^{th} pixel is illuminated can be described by

$$t_i = t_0 + \frac{R_p}{c} \tan\left[(\chi_0 - \chi_i)/2\right]. \tag{3.2}$$

The shower axis is defined by two parameters. The perpendicular distance R_p which is the shortest distance between the telescope and the shower axis with corresponding time t_0 and the angle χ_0 which is spanned by the shower axis and the ground. χ_i is the angle between the ground and the pointing direction of the i^{th} pixel (Fig. 3.6).
The fit of the measured data to equation 3.2 yield the shower parameters R_p and χ_0.

However, in some cases the angular speed $d\chi/dt$ is nearly constant which leads to a poor reconstruction using only the fluorescence detectors. This is shown in Fig. 3.7. The coloured points correspond to the FD data and the fitted curve (red) completely misses the SD data (black squares) while having high uncertainties. To improve the reconstruction a hybrid method is applied in which the timing informations from the SD is used in addition to the FD data which yield much better results.

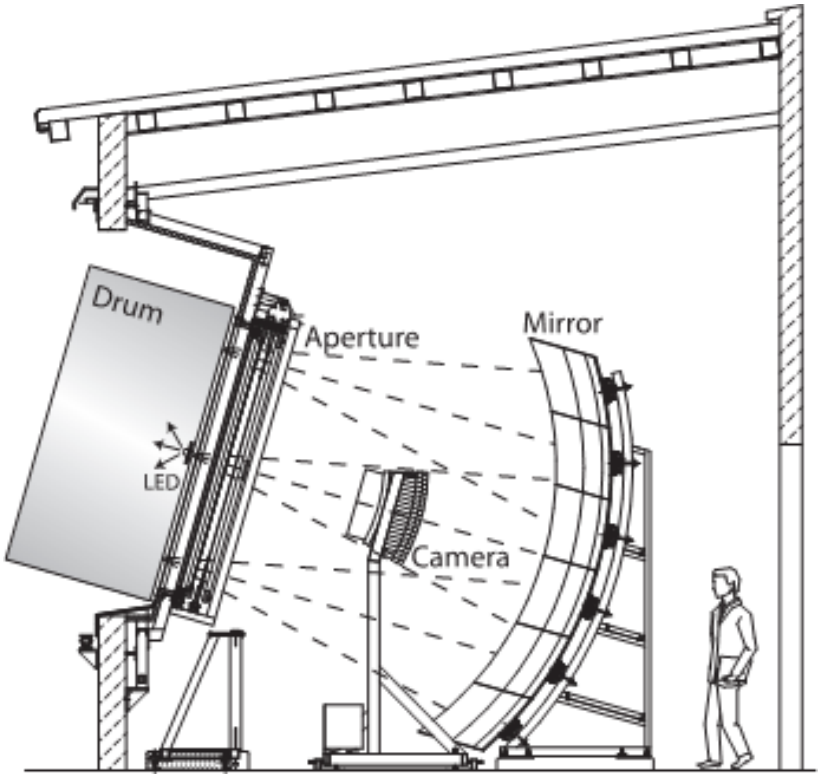

Figure 3.5: Drum calibration source for the FD telescopes. From [19].

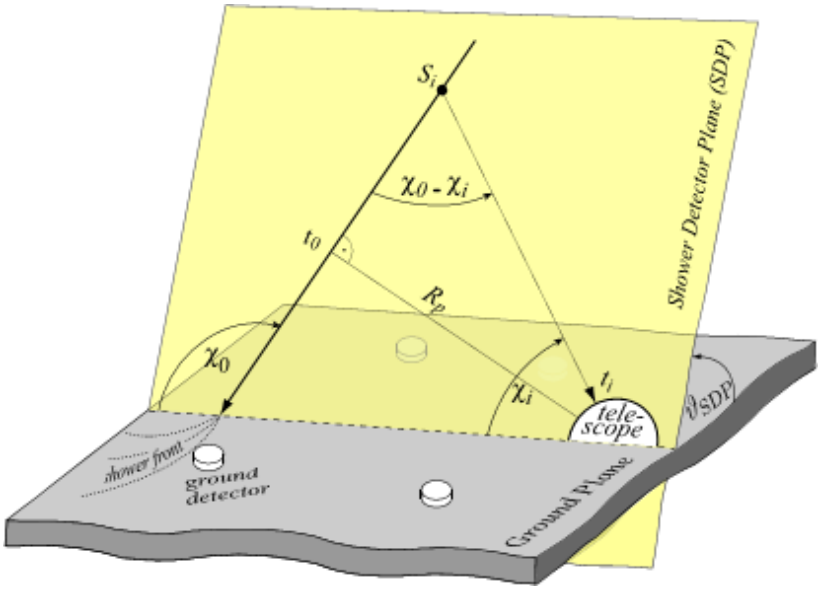

Figure 3.6: Illustration of the geometrical shower reconstruction from the observables of the fluorescence detector. From [19].

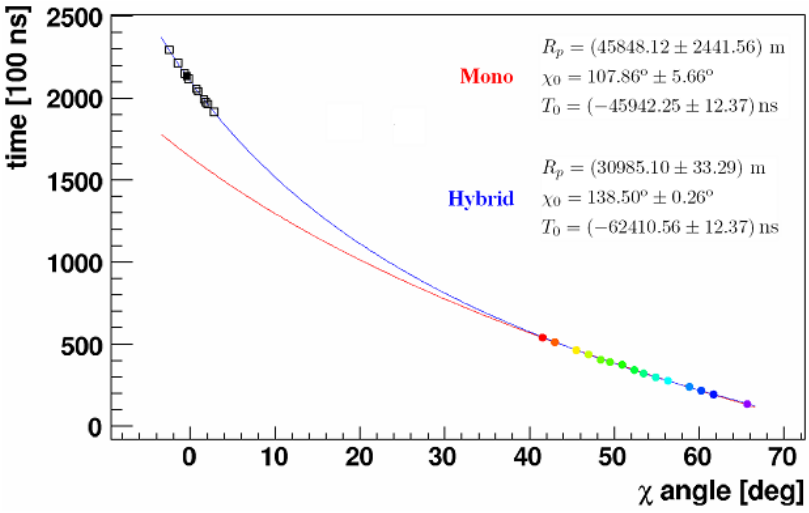

Figure 3.7: Functional form that correlates the time of arrival of the light at each pixel with the angle between the pointing direction of that particular pixel and the horizontal line within the shower-detector plane. FD data (color points) and SD data (squares) are superimposed to the monocular (red line) and hybrid (blue line) reconstruction fits. The full square indicates the SD station with the highest signal. This is a typical event in which the monocular reconstruction does not work well. From [19].

In order to reconstruct the energy of the extensive air shower the proportionality between the number of photons and the energy as stated in equation 3.1 can be used. Then a Gaisser-Hillas function is fitted to the longitudinal energy profile:

$$f_{GH}(X) = \left(\frac{dE}{dX}\right)_{max} \left(\frac{X - X_0}{X_{max} - X_0}\right)^{\frac{X_{max}-X_0}{\lambda}} e^{\frac{X_{max}-X}{\lambda}}. \tag{3.3}$$

The maximum of the shower profile is given by $\left(\frac{dE}{dX}\right)_{max}$ and X_0 and λ are shape parameters of the function. The total energy of the shower results from integrating equation 3.3 while correcting for energy which is invisible to the detector, like high energy muons and neutrinos.

3.3 The High Elevation Auger Telescopes

The flat orientation of the standard fluorescence telescopes and the resulting field of view of only 30° in elevation leads to a bias towards high energy air showers. Primary particles with low energies produce extensive air shower that emit less fluorescence light than showers evolving from high energy primary particles. Furthermore, they develop in higher parts of the atmosphere. In order to be detected by the FD telescopes the shower has to evolve close to the detector site. Due to the flat orientation of the FD telescopes it is very likely that the maximum of the shower X_{max} is above the field of

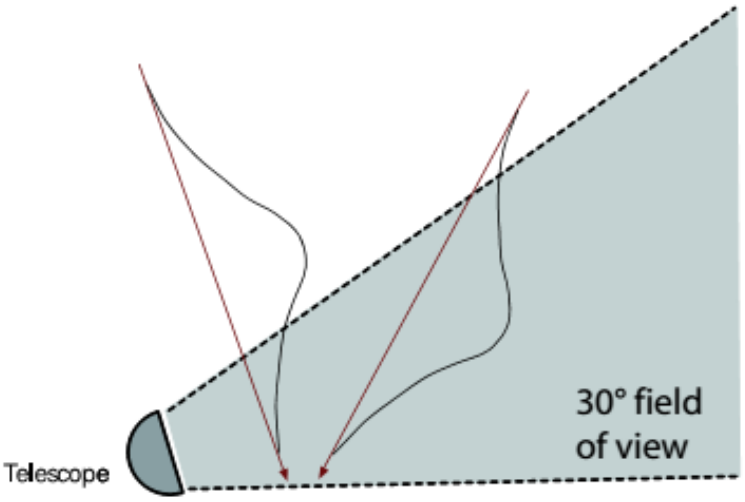

Figure 3.8: Effect of limited field of view on reconstruction: Showers approaching the telescope have much higher reconstruction probability than those departing. From [2].

view (see Fig. 3.8). Additionally there is a bias to favour EAS that develop towards the telescopes, as it is more likely that the shower maximum is in the detectors field of view.

The High Elevation Auger Telescopes (HEAT) were designed to increase the field of view of the fluorescence detector from 0 to 30° up to 60° (Fig. 3.9) and thus to lower the energy threshold by almost one order of magnitude compared to the standard fluorescence telescopes.

HEAT was built close behind the FD site Coihueco to align the fields of view of the telescopes. In front of the FD telescopes the SD array was upgraded as well by adding additional tanks to decrease the spacing between the tanks from 1500 m to 750 m. 3.10

The design for HEAT was adapted from the standard fluorescence telescopes but the whole building was built in such a way that it could be tilted upwards by 30° as shown in Fig. 3.11. In contrast to the standard FD each HEAT telescope has its own, completely tilt-able housing. To ensure, that the optical system is not influenced by the tilting process, the housings are build on a massive ground plate with additional structures to support the camera and the mirror. Furthermore, a monitor system [26] is installed to check for any changes in distance and inclination between the optical instruments.

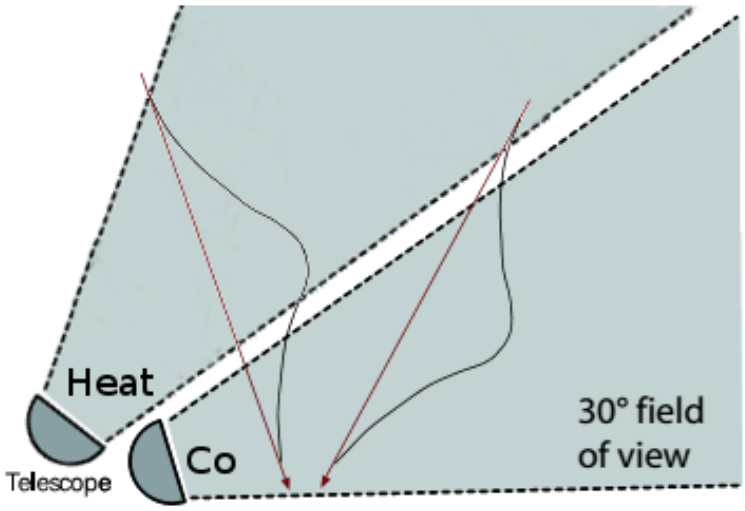

Figure 3.9: Field of view of Coihueco (Co) and HEAT. Adapted from [2].

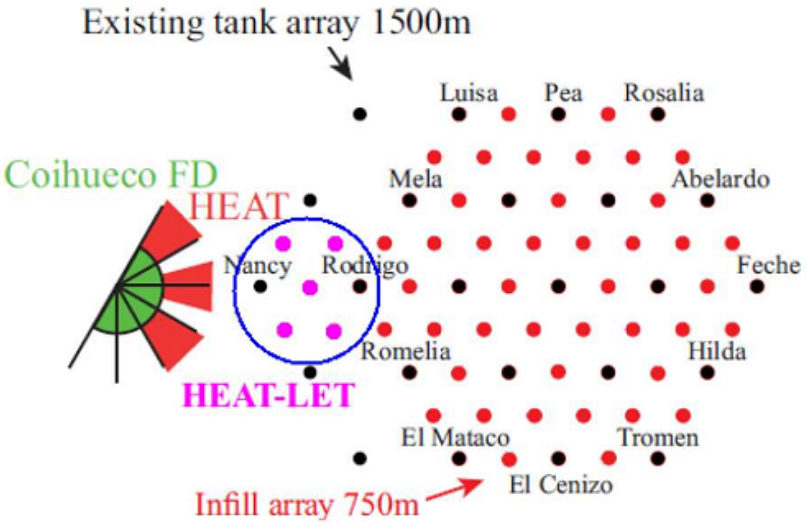

Figure 3.10: Shown is a map of the positions of the AMIGA infill detector stations and the position of the Coihueco and HEAT telescopes. AMIGA is the extension of the SD and HEAT the extension of the FD of the Pierre Auger Observatory. Black points show SD stations of the regular array, for some of them the individual station names are given in black. Red dots show the additional infill SD stations. Pink dots show the 5 HEATLET stations. The field of view of the Coihueco and HEAT telescopes is shown with green and red slices respectively. Shown is the status of the infill at the end of 2011. From [25].

In downward position (Fig. 3.12a) the telescopes are maintained and cross checks with the Coihueco FD telescopes can be performed, as their field of view overlaps in this mode. The hydraulic tilting process takes about two minutes and sets the

Figure 3.11: Picture of the upwards tilted HEAT telescope housings. From [22].

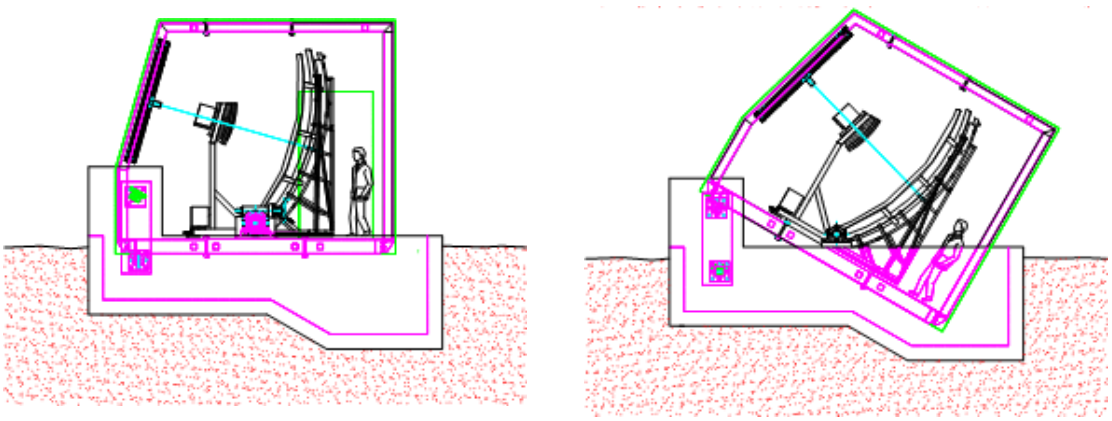

(a) HEAT in downward position

(b) HEAT in upward position

Figure 3.12: Schematic view of the cross-section of one of the HEAT telescopes. Top: Horizontal mode for service and cross-calibration, bottom: data-taking mode in tilted orientation. From [22].

telescopes to the upward, data-taking position (Fig. 3.12b).

Due to the higher event rate expected at HEAT and the higher angular velocities due to the different geometry compared to the standard FD telescopes, the electronics used for HEAT had to be improved. Mainly, the sampling rate was increased from 10 MHz (FD) to 20 MHz (HEAT) which results in a faster readout speed.

4 Air Shower Simulation and Reconstruction

4.1 Conex

In order to simulate extensive air showers Monte Carlo simulations have to be performed. As these simulations require a huge amount of computation time even on large computer clusters, the hybrid simulation software CONEX [3, 27] has been chosen. Analogue to full Monte Carlo simulations like CORSIKA [28], CONEX calculates the first interactions of an extensive air shower using Monte Carlo simulations. With significantly decreasing energy of the secondary particles the simulations method changes from Monte Carlo simulations to a numerically solution of the cascade equations. The fast, one-dimensional simulations of CONEX provide longitudinal shower profiles as well as further shower parameters which are in good agreement with full Monte Carlo simulations.

This analysis uses CONEX version 2r4.37. Simulations are performed for different hadronic interaction models, QGSJETII-04 [29] and EPOS-LHC [30].

For the response matrix (chapter 6.1) a total of 960,000 air showers were simulated equally split for both interaction models. Within the models two primary particles are considered, proton and iron. The CONEX showers are simulated for an energy regime of $lg\frac{E}{eV} = 16.3 - 18.6$ in equidistant bins of $lg\frac{E}{eV} = 0.1$ bin size resulting in 24 bins. An example is given in fig. 4.1a.

A second set of CONEX showers were generated to test the unfolding algorithms. Therefore a power spectrum with spectral index of $\alpha = 2.7$ was assumed and a total of 800,000 showers were simulated, again split among the two interaction models and the two primary particle types. An example is given in fig. 4.1b.

All simulations were performed for an uniform particle flux on a flat surface in a zenith angle range between 0 and 65° which is represented by the distribution $\frac{dN}{d\cos\theta} \propto \cos\theta$. Zenith angle distributions for each set of simulations are shown in fig. 4.2.

The distribution in azimuth is drawn uniform from 0 to 360°. Fig. 4.3 shows the

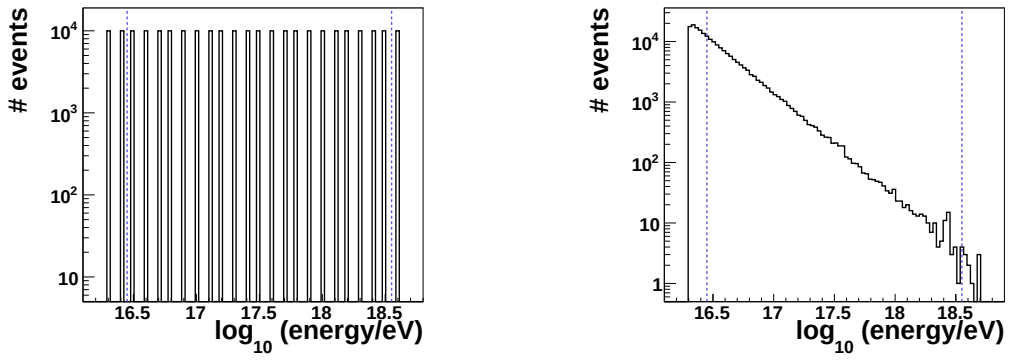

(a) Data sample for response matrix. **(b)** Test sample.

Figure 4.1: Energy distribution of simulated showers (Primary particle H, interaction model QGSJETII-04).

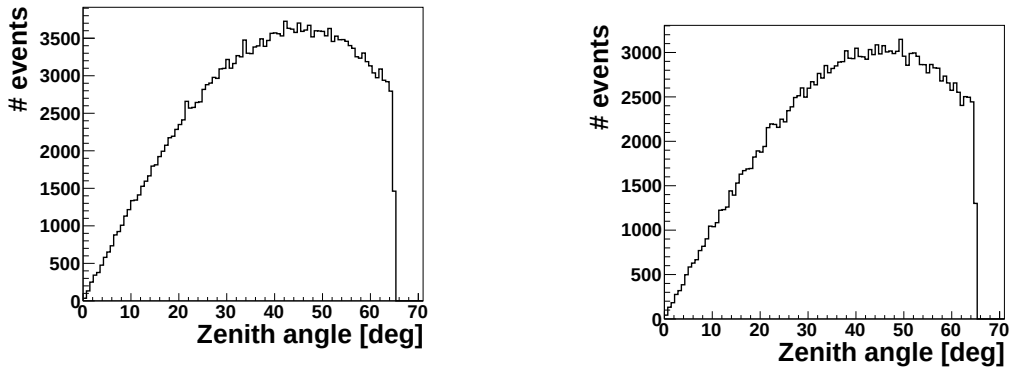

(a) Data sample for response matrix with 240,000 events. **(b)** Test sample with 200,000 events.

Figure 4.2: Zenith angle distribution for simulated showers (Primary particle H, interaction model QGSJETII-04).

distribution for two examples from each MC set.

The further simulation and the reconstruction are performed by the Offline framework which will be described in the following chapter.

4.2 Offline

In order to simulate and reconstruct extensive air showers the Offline framework [4] developed by the Pierre Auger collaboration is used in its version v2r9p1-Valentine. This framework provides a detailed simulation of the detector as well as simulations for

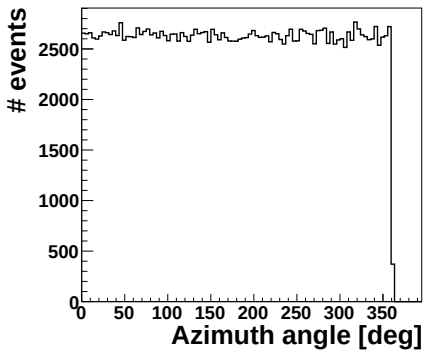

(a) Data sample for response matrix 240,000 events.

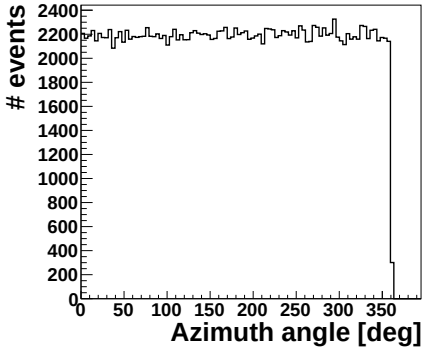

(b) Test sample with 200,000 events.

Figure 4.3: Azimuth angle distribution for simulated showers (Primary particle H, interaction model QGSJETII-04).

the air shower and the atmosphere above the detector. Offline is built in a modular structure where each module can be controlled by XML steering files.

The complete simulation and reconstruction process is operated through a steering file which can call and loop over the individual modules. The steering file for this analysis is presented in section A in the appendix.

In the following section a brief description of the used modules will be given.

4.2.1 Event Simulation in Offline

The standard read-in module **EventFileReaderOG** is used to import the showers created by CONEX individually. This module can also be used to read the Auger raw data as well as many other output formats of different simulation packages like Corsika[28] and Aires[31]. To eliminate non-physical showers the **MCShowerCheckerOG** is executed.

Each shower then receives an event time and a foot point. As low energy extensive air showers emit less fluorescence light, only shower close to the detector can be detected. Therefore, the maximum distance of the shower to the detector is increasing with energy. All showers are simulated in a segment of a circle which is centred in front of HEAT and spans 120° in azimuth. The inner radius corresponding to the minimum distance to the detector is set to be 1000 m. The maximum distance ranges from 6000 m for shower with an energy of $lg\frac{E}{eV} = 16.3$ up to 40,500 m for the highest energy bin simulated ($lg\frac{E}{eV} = 18.6$). The numbers are chosen considering the distances to the detector of real measured events as shown in fig. 4.4.

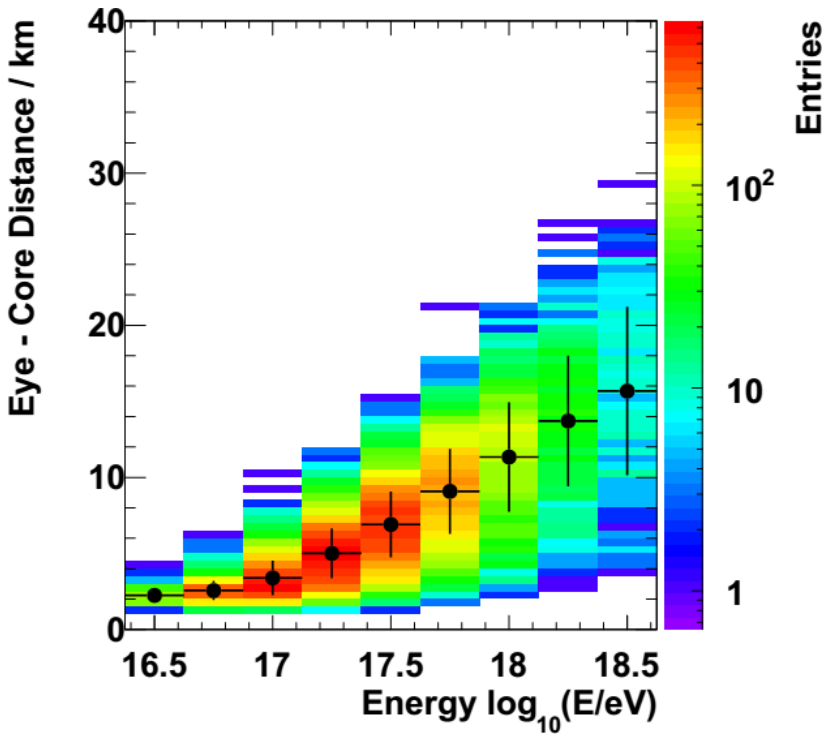

Figure 4.4: This figure shows the distributions of distances from the detector to the shower core in dependence of the shower energy for COHE data. The black dots give the mean of the distribution per energy bin. The horizontal error bars give the bin width and the vertical error bars give the standard deviation. Only basic quality cuts were used. From [25].

In the test MC sample the maximum distance to the detector has to be fixed to 40500 m as the energy of the shower is simulated continuously between $lg\frac{E}{eV} = 16.3$ and $lg\frac{E}{eV} = 18.6$.

To make sure all FD telescopes including HEAT are working the **FdSimEventCheckerOG** is used. Starting the actual shower simulation the **ShowerLightSimulatorKG** simulates the light generation within the air shower. The **LightAtDiaphragmSimulatorKG** calculates the number of photons hitting the diaphragm of the detector by propagating the light through the atmosphere and checking which part of the shower is in the field of view of the detector. Expanding the one-dimensional shower profile with the lateral component of the energy deposit is acquired by using the **ShowerPhotonGeneratorOG**. The transition of the photons from the telescope diaphragm to the PMT camera is simulated by the **TelescopeSimulatorKG** module. It takes into account all details of the detector up to the material reflectivity and transmission. Background to the FD telescopes is mainly due to star and moon light and is simulated in the **FdBackgroundSimulatorOG** module. As these sources of background do not change significant during the time scale of a single air shower it essentially raises the baseline of the signal. Sampling and electronics are simulated in

the **FdElectronicsSimulatorOG** module before finishing the FD detector simulation by applying the FD triggers in the **FdTriggerSimulatorOG** module.
All necessary simulations concerning the SD part of the detector are performed by the **SdSimpleSimKG** module.
The **CentralTriggerSimulatorXb** and **CentralTriggerEventBuilderOG** modules represent the CDAS (Central Data Acquisition System) and together generate a hybrid SD and FD event.
Finally, all informations and simulation results are stored in an $\overline{\text{Off}}\underline{\text{line}}$ event by the **EventBuilderOG** module.

After finishing the event simulation part of the $\overline{\text{Off}}\underline{\text{line}}$ module sequence, the reconstruction part can be started. As the reconstruction can be performed immediately after the simulation the events do not have to be read-in again. In case of measured data or if the simulation and the reconstruction have to be separated the EventFileExporter module has to be used at the end of the simulation to store the data. Also, to read-in the data at the beginning of the reconstruction the EventFileReader module has to be applied.

The reconstruction is started by the **EventCheckerOG** module which tries to find broken events due to missing timing or detector information stored among the events. To convert the signal measured by the detectors which is stored as FADC traces into photon counts, the **FdCalibratorOG** module applies the calibration constants for the different telescopes. Afterwards, the information from the individual telescopes are merged into one virtual eye by the **FdEyeMergerKG** module. The eye which is used in this analysis that contains the three HEAT telescopes as well as the FD site Coihueco is called COHE. The modules **FdPulseFinderOG** and **FdSDPFinderOG** find the maximum signals in each pixel and fit the shower detector plane (see section 3.2) to the data. To reconstruct the precise geometry of the shower the modules **FdAxisFinderOG**, **HybridGeometryFinderOG** and **HybridGeometryFinderWG** are used. After receiving a preliminary shower axis by analysing the timing information of the pixels, additional timing informations from one SD station that triggered are used to reconstruct a more precise shower axis. Subsequently the light flux at the aperture of the telescope is calculated by the **FdApertureLightKG** module. Finally, the **FdEnergyDepositFinderKG** can calculate the energy deposit profile from which the shower maximum and the total energy deposit can be calculated. Therefore a Gaisser-Hillas profile is fitted to the profile. The total energy yields from the integral of the Gaisser-Hillas function while taking into account the energy not recorded due to neutrinos. The data is then written into an ADST (Advanced Data Summary Tree [32]) output file by the **RecDataWriterNG**. Additionally many informations about the reconstruction process are stored in the file as well.

4.3 Applied cuts

After completing the reconstruction multiple cuts are applied to the MC data. These cuts are the same cuts as in [25] as this analysis will be applied to the data of the mentioned publication. To build a responsematrix that is capable of representing the detector that measured the mentioned data, the same analysis has to be applied.
The cuts are performed by the selectEvents program that comes with the ADST-Analysis toolkit [32].

The cut steering file is printed in the appendix in sectionB. A short description will be given in the following section.

Out of all stored events, only those with a successful energy reconstruction are considered (**hasEnergy**). Furthermore, the accepted events have to be so called hybrid events (**isHybrid**), which use SD timing informations in the reconstruction of the shower geometry. The **eyeCut** checks for the detector the shower has triggered. Only showers that develop in the field of view of both, Coihueco and HEAT are considered. This virtual eye is called COHE. Also, geometric parameters like the maximum zenith angle (**maxZenithFD**) which should not exceed 60°, and the maximum distance of the foot point to the next SD station (**maxCoreTankDist**) are checked. As the SD stations are positioned in an hexagonal array with maximum distance of 1500 m the cut value of 800 m only corresponds to events which have their foot points outside the SD array. The quality of the reconstruction is examined by rejecting events with a high relative uncertainty on the energy reconstruction (**energyError**). Another limiting factor to a successful reconstruction is the fraction of Cherenkov light. Events with an Cherenkov-fraction exceeding 50% are therefore rejected (**maxDirCFrac**). This fraction is higher for events measured with the HEAT telescopes compared to the standard FD telescopes as it is more likely for showers to point right into the detector stations due to the changed geometry of the telescopes.
Additionally the measured profile has to satisfy certain conditions to be accepted. The shower maximum has to be in the field of view of the telescopes and is not allowed to be too close to the borders (**xMaxInFOV**). The quality of the fit is also checked by the χ^2/NDF value of the Gaisser-Hillas fit to the data (**profileChi2**). Holes, which may occur in the shower profile are only allowed if they are small compared to the total track size (**maxDepthHole**). It is important to allow for these holes to appear, because besides clouds that might evoke them, they also appear due to the gaps between the field of view of the standard FD and the HEAT telescopes.
Finally two boolean cuts are applied which reject events with saturated pixels (**skipSaturated**) which is most important for high energy showers as well as events with bad pixels (**!badPixels**) which corresponds to non operative pixels. The latter do not occur in simulated data as all pixels are assumed to work in the detector simulation.

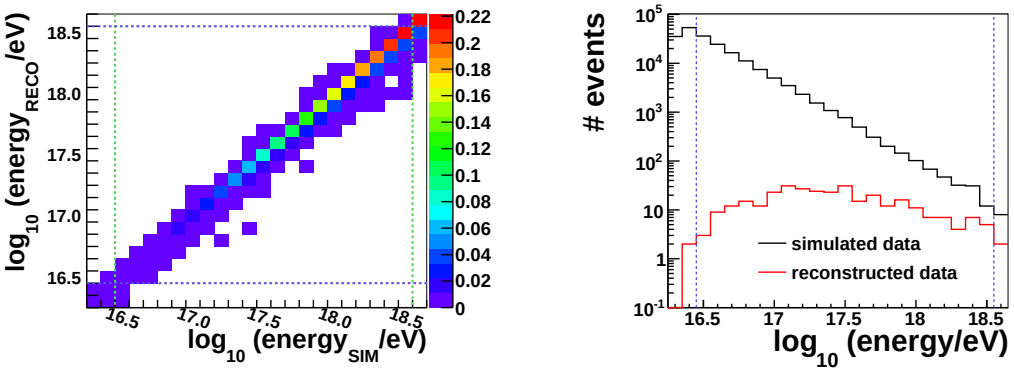

(a) Response matrix sample. **(b)** Test sample.

Figure 4.5: Distribution of pseudo-measured events after cuts. Primary H, QGSJET-II.

This cut has been taken into account for consistency.

Fig. 4.5 shows the distribution of the pseudo-measured events after applying all the cuts mentioned before.

5 Unfolding of distributions

5.1 Introduction

Every detector used in particle physics has a finite resolution and a limited acceptance. Therefore, the data measured by the detector is always distorted and can not be compared easily with data obtained from other experiments.

The distribution of the measured data can be filled into a vector b. Each entry of the vector corresponds to one of the n_b bins of the distribution. Likewise a vector x of the true data distribution of dimension n_x can be defined. The transition from the true data to the measured data can now be parametrized with a $n_b \times n_x$ matrix A:

$$Ax = b. \tag{5.1}$$

Using Monte Carlo methods we can simulate an initial true distribution x^{ini}. After applying the detector simulation to x^{ini} we get the measured distribution b^{ini} which leads to a system of linear relations for the true and the measured distribution:

$$Ax^{ini} = b^{ini}. \tag{5.2}$$

With a measured distribution b and the response matrix A from Eq. 5.2 one can now calculate the underlying true distribution x according to Eq. 5.1. A naive matrix inversion of the matrix A would only be possible if $n_x = n_b$ and even then the result would be highly fluctuating due to the finite resolution and the limited acceptance.

Therefore advanced methods have to be applied in order to solve this ill-posed problem.

5.2 Bayes Unfolding

The unfolding method called Bayes unfolding was first introduced by Giulio D'Agostini in 1995. [5] In contrast to simple bin-by-bin unfolding this method takes into account the possible migration of events between adjacent bins.

In order to describe this method the terms causes (C) and effects (E) are used. Causes are related to the true values, which are not smeared, whereas effects correspond to the values measured by the detector. As shown in Fig. 5.1 effects and causes can not be linked unambiguous due to efficiency and resolution as well as migration and statistics. Also a trash bin is introduced which accounts for events that does not end

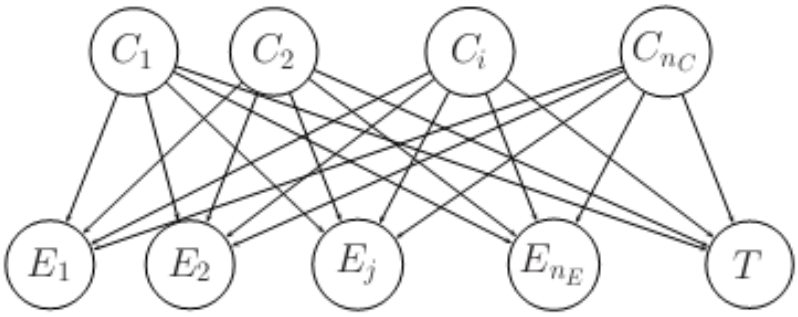

Figure 5.1: Connections between the causes (C) and effects (E), taking into account a trash bin (T). From [33]

up in any effect bin. Though, with Monte Carlo studies we can estimate the probability that the cause C_i induces the effect E_j: $P(E_j|C_i)$.

With the help of Bayes' Theorem (5.3) we can calculate the probability $P(C_i|E_j)$ which tracks back the effects to the causes.

$$P(C_i|E_j) = \frac{P(E_j|C_i) \cdot P_0(C_i)}{\sum_{l=0}^{n_C} n(P(E_j|C_l)) \cdot P_0(C_l)} \tag{5.3}$$

This probability enables us to calculate the expected number of events in the cause bin i from the distribution of the effects $n(\mathbf{E})$ as well as the efficiency ϵ_i of the causes which is necessary because some causes may lead to effects that are not registered by the detector. In Fig. 5.1 this is illustrated by the trash bin T.

$$\hat{n}(C_i) = \frac{1}{\epsilon_i} \sum_{j=1}^{n_E} n(E_j) \cdot P(C_i|E_j) \qquad \epsilon_i \neq 0 \tag{5.4}$$

The result of Eq. 5.4 strongly depends on the initial distribution of the causes, which usually is unknown. To minimize this influence an iterative method is introduced.

Therefore we start with some arbitrary distribution $P_0(C_i)$ and apply Eq. 5.3 and Eq. 5.4. Here we choose the MC truth distribution for $P_0(C_i)$.
From the true number of events from Eq. 5.4 we can calculate a new distribution $P(C_i)$ and iterate the process.
To prevent the results from starting to oscillate some sort of regularization has to be performed. This is achieved by stopping the iteration after few repetitions. Also applying some sort of smoothing of the distribution between iterations is possible but not performed in this work.

5.2.1 Uncertainty estimation

In order to calculate the uncertainties for the unfolded distribution $\hat{n}(C_i)$ the error propagation matrix has to be computed. Therefore one can rewrite eq. 5.4 in terms of all relevant quantities.

$$\hat{n}(C_i) = \sum_{j=1}^{n_E} \frac{P(E_j|C_i n_0(C_i))}{\epsilon_i f_j} n(E_j) = \sum_{j=1}^{n_E} M_{ij} n(E_j) \tag{5.5}$$

From this equation one can calculate the error propagation matrix:

$$\frac{\partial \hat{n}(C_i)}{\partial n(E_j)} = M_{ij} + \sum_{k=1}^{n_E} M_{ik} n(E_k) \left(\frac{1}{n_0(C_i)} \frac{\partial n_0(C_i)}{\partial n(E_j)} - \sum_{l=1}^{n_C} \frac{\epsilon_l}{n_0(C_l)} \frac{\partial n_0(C_l)}{\partial n(E_j)} M_{lk} \right) \tag{5.6}$$

This equation does not only take into account the error propagation of $n(E_j)$ but also the dependence of $n(E_j)$ of the matrix M_{ij}. In case of the first iteration $\frac{\partial n_0(C_i)}{\partial n(E_j)} = 0$ and only the first part of Eq. 5.6 does not vanish. For subsequent iterations $\frac{\partial n_0(C_i)}{\partial n(E_j)} = 0$ corresponds to $\frac{\partial \hat{n}(C_i)}{\partial n(E_j)}$ of the previous iteration.

With the error propagation matrix Eq. 5.6 the covariance matrix

$$V(\hat{n}(C_k), \hat{n}(C_l)) = \sum_{i,j=1}^{n_E} \frac{\partial \hat{n}(C_k)}{\partial n(E_i)} V(n(E_i), n(E_j)) \frac{\partial \hat{n}(C_l)}{\partial n(E_j)} \tag{5.7}$$

can be calculated using the covariance matrix $V(n(E_i), n(E_j))$ of the measured distribution.

5.3 Singular Value Decomposition

Another method to perform unfolding is the so called Singular Value Decomposition which is documented by A. Höcker and V. Kartvelishvili in [6].

Starting from Eq. 5.1 one can factorise the matrix A into three matrices $A = USV^T$. U and V are orthogonal matrices with U being an $m \times m$ matrix and V being a $n \times n$ matrix. The $m \times n$ matrix S is diagonal and contains the singular values $s_{ii} = s_i$ which are ordered from high values to low values.

Using the factorisation equation 5.1 can be rewritten as follows:

$$Ax = b \tag{5.8}$$

$$USV^T x = b \tag{5.9}$$

$$Sz = d \tag{5.10}$$

In Eq. 5.10 $z = V^T x$ and $d = U^T b$ has been introduced. As all off-diagonal elements of S are equal to zero Eq. 5.10 can also be written as $s_i z_i = d_i$. Thus, z can be calculated by $z_i = d_i/s_i$. One can see that small singular values s_i amplify the errors in d_i.

In order to solve this problem Eq. 5.1 has to be rescaled by the true MC distribution x_i^{ini}. Furthermore the resulting equation has to be divided by the error of b. This leads to

$$\tilde{A}_{ij} w_j = \tilde{b}_i \tag{5.11}$$

with $w_i = x_i/x_i^{ini}$.

Applying the same steps as in Eq. 5.8-5.10 with $z = V^T w$ and $d = U^T \tilde{b}$.
The solution of $\tilde{A}_{ij} w_j = \tilde{b}_i$ can be found by minimizing the χ^2 function

$$\chi^2 = (\tilde{A}w - \tilde{b})^T (\tilde{A}w - \tilde{b}) = min \tag{5.12}$$

As this solution would still feature rapid oscillations a regularization term $\tau(Cw)^T(Cw)$ has to be introduced. The choice of Cw being the second finite derivative corresponds to the assumption of a smooth solution.

$$(Cw)^T(Cw) = \sum [(w_{i+1} - w_i) - (w_i - w_{i-1})] \tag{5.13}$$

The final Ξ^2 term that has to be minimize reads:

$$\Xi^2 = (\tilde{A}w - \tilde{b})^T (\tilde{A}w - \tilde{b}) + \tau(Cw)^T Cw = min \tag{5.14}$$

This problem can be reduced to the old one by transforming the equation into an matrix equation:

$$\begin{bmatrix} \tilde{A}C^{-1} \\ \sqrt{\tau} \cdot I \end{bmatrix} Cw = \begin{bmatrix} \tilde{b} \\ 0 \end{bmatrix} \tag{5.15}$$

In the case of $\tau = 0$ one immediately sees that Eq. 5.15 becomes equal to Eq. 5.11, which can be solved using the singular value decomposition. The solution in this case is

$$z_i^(0) = \frac{d_i}{s_i}, \tag{5.16}$$

$$w^0 = C^{-1} V z^(0). \tag{5.17}$$

The solution of the full equation 5.15 can now be found by using a method described by Lawson and Hanson [34]. They verify, that the solution of 5.15 can be deduced from the $\tau = 0$ case by substituting d_i in the following manner:

$$d_i^(\tau) = d_i \frac{s_i^2}{s_i^2 + \tau}. \tag{5.18}$$

Therefore, the regularized equation yield the solution

$$z_i^{(\tau)} = \frac{d_i s_i}{s_i^2 + \tau}, \tag{5.19}$$

$$w^{(\tau)} = C^{-1} V z^{(\tau)}. \tag{5.20}$$

The effect of τ can be described by a typical low-pass filter with the cut-off value τ. In order to apply a reasonable regularization τ has to be chosen adequately. Höcker and Kartvelishvili recommend to choose $\tau = s_k^2$ with k corresponding to the last significant d.

Uncertainty estimation

The covariance matrices of eq. 5.19 and 5.20 follow immediately:

$$Z_{ik}^{(\tau)} = \frac{s_i^2}{(s_i^2 + \tau)^2} \cdot \delta_{ik}, \tag{5.21}$$

$$W^{(\tau)} = C^{-1} V Z^{(\tau)} V^T (C^{-1})^T. \tag{5.22}$$

Furthermore, the covariance matrix of the unfolded distribution

$$x_i^{(\tau)} = x_i^{ini} w_i^{(\tau)} \tag{5.23}$$

can be calculated with 5.22:

$$X_{ik}^{(\tau)} = x_i^{ini} W_{ik}^{(\tau)} x_k^{ini}. \tag{5.24}$$

6 Analysis of the energy spectrum

6.1 The response matrix

The response matrix represents the behaviour of the detector. It is build by using Monte Carlo simulations to study the response of the detector towards well-defined incoming events. For each interaction model (QGSJETII-04 and EPOS LHC) as well as for each primary particle type (proton and iron) an independent response matrix is filled with 240,000 simulated events each (see section 4.1).

The simulated distribution, which is a flat distribution between $lg\frac{E}{eV} = 16.3 - 18.6$ with 10,000 events per bin, and the reconstructed signal are shown in fig. 6.1 for each MC sub-sample. In the analysis itself a smaller energy regime ($lg\frac{E}{eV} = 16.5 - 18.5$) has been used to minimize the influence of migration effects that occur on the border the matrices.

The response matrix can then be build by filling each event into the corresponding bin with respect to its reconstructed and simulated energy ($E_{reconstructed}$,$E_{simulated}$). Fig. 6.2 shows the four response matrices generated for this analysis.

6.2 Compare methods using reconstructed Monte Carlo data

To evaluate the different unfolding methods and to find the best fitting regularization parameters the unfolding was tested on MC samples. For each interaction model and each primary particle type a test MC sample of 200,000 events was generated as described in sec. 4.1 and sec. 4.2. Furthermore, the same cuts (sec. 4.3) were applied. The resulting distributions are shown in fig. 6.3. Again a larger energy regime $lg\frac{E}{eV} = 16.3 - 18.6$ than actually used was simulated to minimize the influence of effects at the border of the histograms.

The further analysis will first be described with figures from the sub-sample of the hadronic interaction model QGSJETII-04 and H as primary particle.

In the first instance the Bayes unfolding method will be studied.

The results of the unfolding algorithm after one iteration are shown in fig. 6.4a

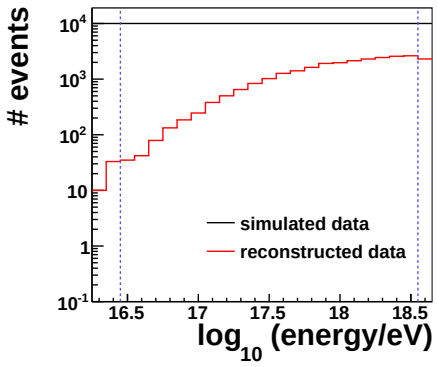

(a) QGSJETII-04, primary H.

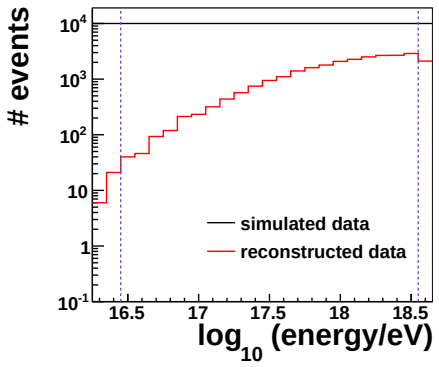

(b) QGSJETII-04, primary Fe.

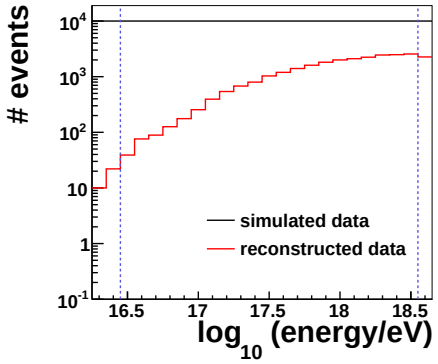

(c) EPOS LHC, primary H.

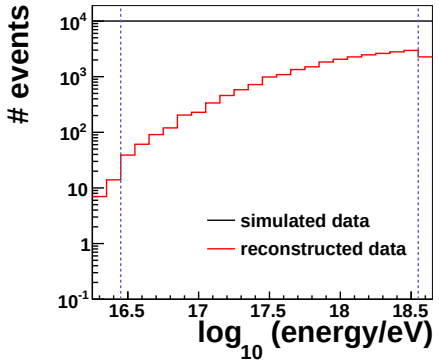

(d) EPOS LHC, primary Fe.

Figure 6.1: Simulated true (black) and reconstructed (red) distributions.

as well as the difference between the unfolded and the simulated (true) distribution normalized to the latter. Furthermore, the correlation matrix of the resulting distribution is given in fig. 6.4b.

One can see, that aside the bins at the border of the energy regime, the unfolded spectrum reproduces the simulated spectrum very good. The correlation matrix is highly diagonal and only small correlations occur in the lowest bins.

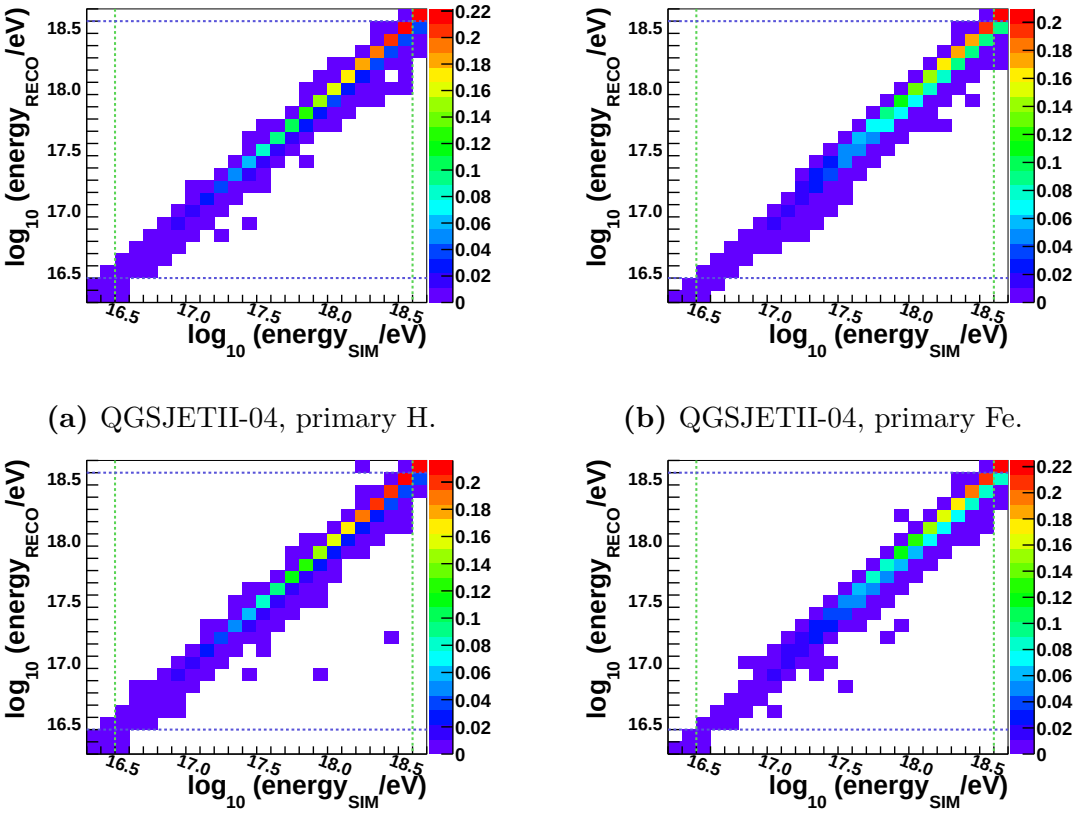

(a) QGSJETII-04, primary H.

(b) QGSJETII-04, primary Fe.

(c) EPOS LHC, primary H.

(d) EPOS LHC, primary Fe.

Figure 6.2: Response matrices generated for this analysis. The dashed lines mark the energy regime used for the analysis.

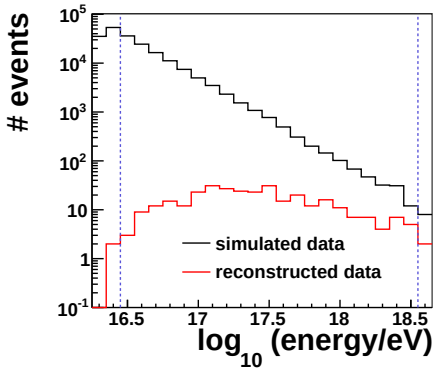

(a) QGSJETII-04, primary H.

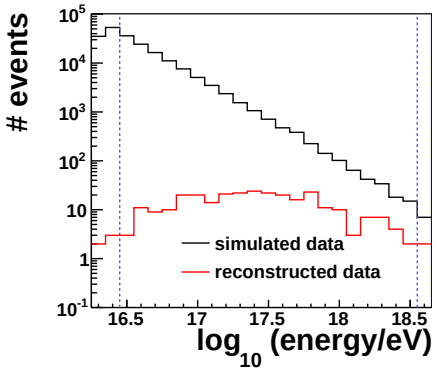

(b) QGSJETII-04, primary Fe.

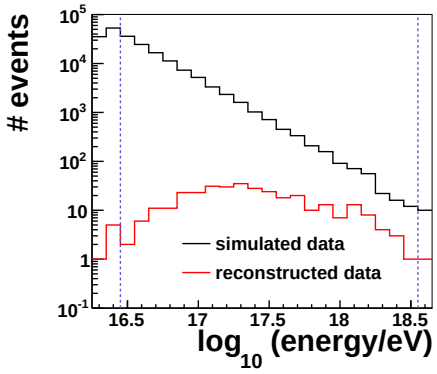

(c) EPOS LHC, primary H.

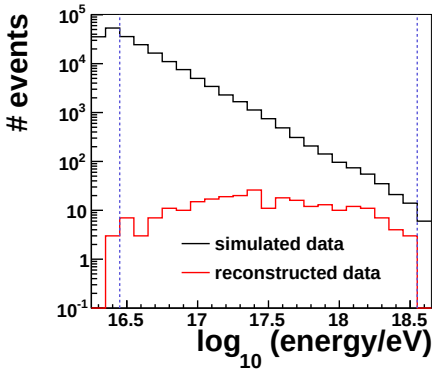

(d) EPOS LHC, primary Fe.

Figure 6.3: Simulated true (black) and reconstructed (red) distributions for the test of the unfolding algorithms.

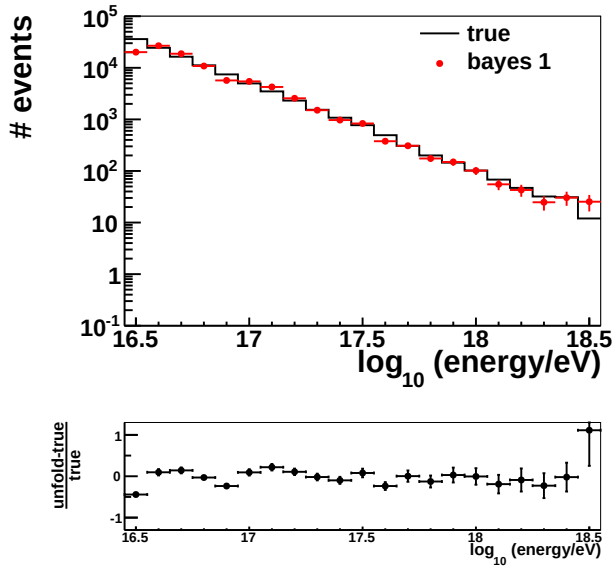

(a) Simulated true(black)and reconstructed (red) distribution for the test of the unfolding algorithm.

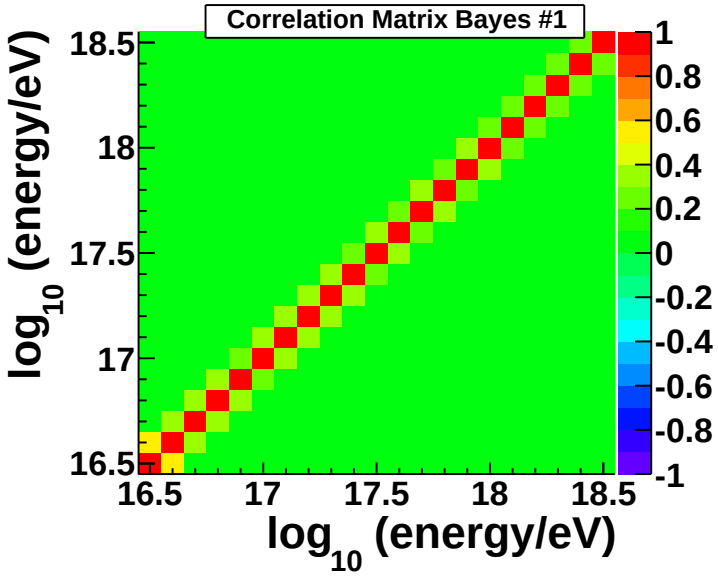

(b) Correlation matrix.

Figure 6.4: Results for the unfolding of the test distribution with one iteration of Bayes Unfolding.

To introduce a measure for the reconstruction, a χ^2 test [35] and a Kolmogorov-Smirnov Goodness-of-Fit [36] test are applied which will be described briefly.

χ^2 test

To compare the unfolded with the initial simulated distribution a χ^2 test is performed. This type of statistical test was first introduced by Pearson in 1904 [37].

Given the unfolded distribution $x_{unfolded}$ and the simulated distribution $x_{simulated}$, the χ^2 value corresponds to the sum over the difference of $x_{unfolded}$ and $x_{simulated}$ weighted with the inverse of the covariance matrix V. This can be written as:

$$\chi^2 = (x_{unfolded} - x_{simulated})^T V^{-1} (x_{unfolded} - x_{simulated}). \tag{6.1}$$

Kolmogorov-Smirnov Goodness-of-Fit test

The Kolmogorov-Smirnov (K-S) test [36] makes use of the so called empirical distribution function (ECDF). The ECDF counts the data points (N) and adds the value 1/N at the position of each data point resulting in a step function with an y-range from 0 to 1:

$$E_N = n(i)/N. \tag{6.2}$$

$n(i)$ corresponds to number of all points which have lower values then the i^{th} data point.
The ECDF as well as the normal cumulative distribution function are plotted for a sample of 100 normal random numbers and shown in fig. 6.5.

The test statistic **D** is the maximum distance between the ECDF of the tested distribution and the theoretical cumulative distribution (F). It is defined to be

$$D = \max_{1 \le i \le N} \left(F(Y_i) - \frac{i-1}{N}, \frac{i}{N} - F(Y_i) \right), \tag{6.3}$$

where Y_i represent the data points.

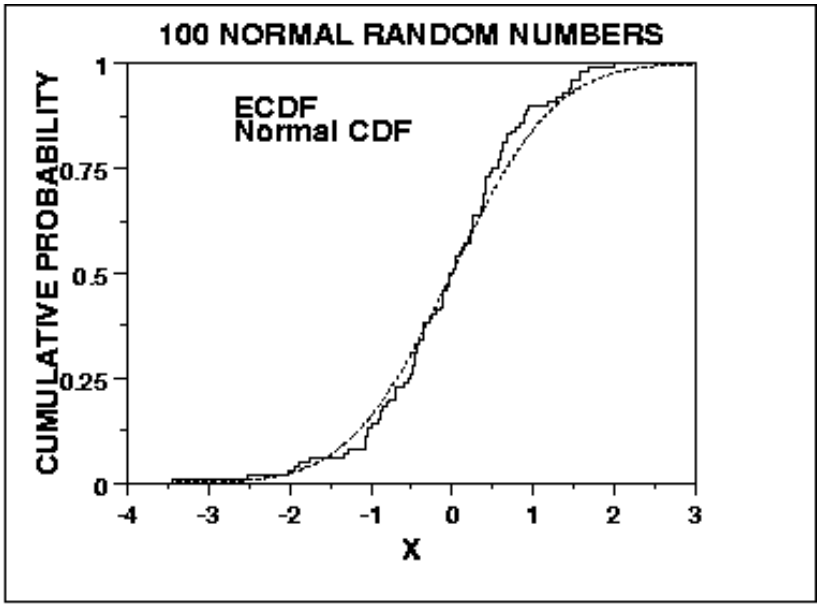

Figure 6.5: Plot of the empirical distribution function (solid) with a normal cumulative distribution function (dashed) for 100 normal random numbers. From [36].

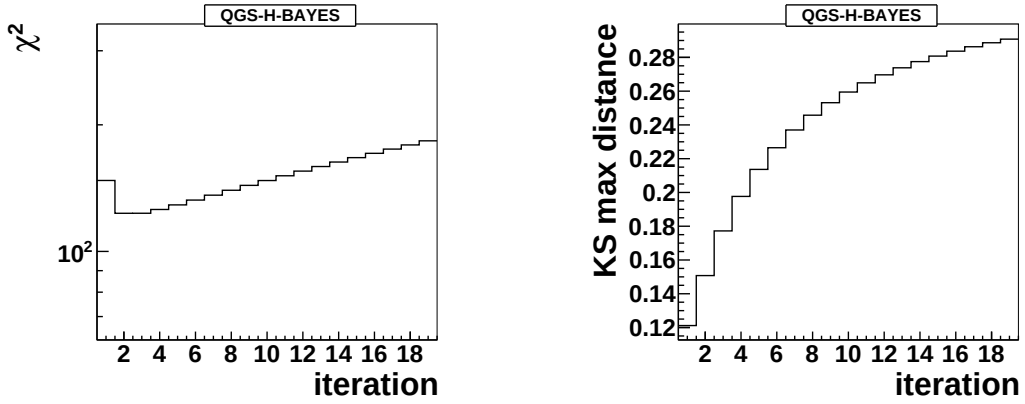

(a) χ^2 test results.

(b) K-S test results.

Figure 6.6: Results of the stochastic test methods applied to the unfolded spectrum using Bayes Unfolding. QGSJETII-04, primary H.

6.2.1 Bayes Unfolding

The unfolding of the test MC sample was performed with regularization parameters varying from one to 20 iterations. For each unfolded spectrum, both χ^2 and K-S test have been carried out with respect to the simulated distribution. The results are given in fig. 6.6a for the χ^2 test and fig. 6.6b for the K-S test.

One can see, that for both tests the best results are obtained for low regularization parameters.

In order to combine both tests and find the best overall regularization parameter the χ^2 test value and the K-S test value are plotted against each other. At each point the corresponding regularization parameter is plotted. Ideally the points should arrange in an L shape with the best regularisation parameter at the bottom left kink. Therefore this type of plot is called L-curve. The result is given in 6.7. The regularization parameter in the lower left corner (2 iterations) yields the best regularization parameter.

The results for one to four iterations are shown in fig. 6.8 together with their deviation from the simulated distribution (fig. 6.8b). Furthermore, the correlation matrices for these for results are given in fig. 6.9.

One can see, that for one iteration (fig. 6.9a) positive correlations occur in the lowest energy bins. At four iterations, negative correlations at the elements next to the diagonal start to arise. The best regularization parameter therefore is 2.

In case of EPOS-LHC and H as the primary (see fig. 6.10) the χ^2 value does decrease slightly with the number of iterations while the K-S test statistic rapidly. The best overall regularization parameter, which appears to be two, can be taken from the

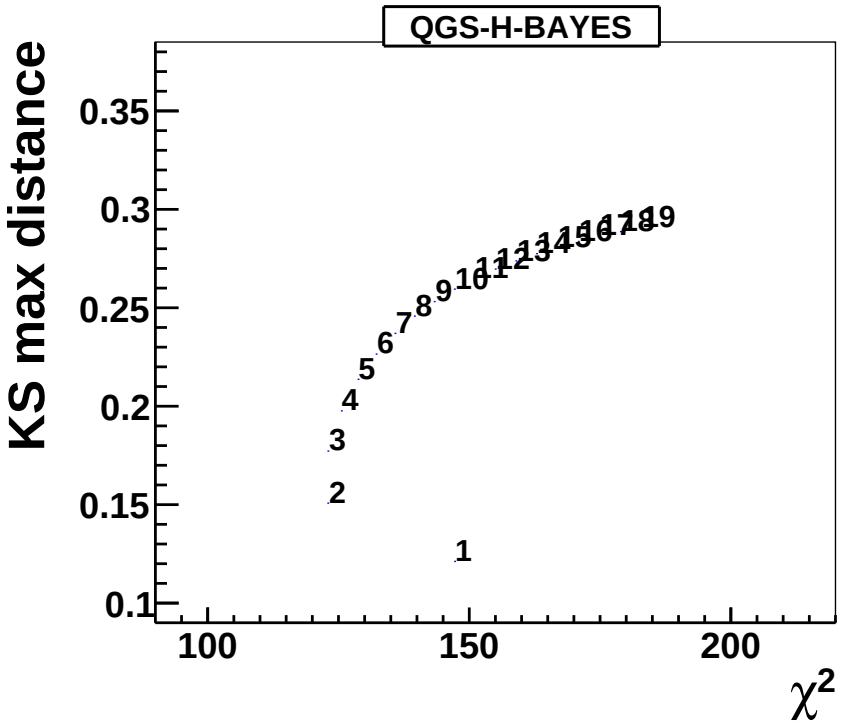

Figure 6.7: QGSJETII-04, primary H.

Model Primary	QGSJETII-04	EPOS-LHC
H	2	2
Fe	2	2

Table 1: Regularization parameters for Bayes Unfolding.

L-Curve (fig. 6.10). The correlation matrices (fig. 6.11) support this choice.

The two test samples with iron as primary particles show a similar behaviour in terms of the L-curve (fig. 6.12). Each one starts at high χ^2 values and low **D** values and ends vice versa. Therefore the L-curves do not show any distinctive kink. Plotting the first few results for low numbers of iteration one can see, that the difference between the unfolded and the simulated data, especially in the lowest and highest bins increases with the number of iterations. The typical property of an under regularized unfolding, which is the oscillation of the unfolded data around the true distribution do become obvious in fig. 6.13c and fig. 6.13d. This fact and the correlation matrices (fig.6.14 and fig. 6.15) favour small regularization factors.

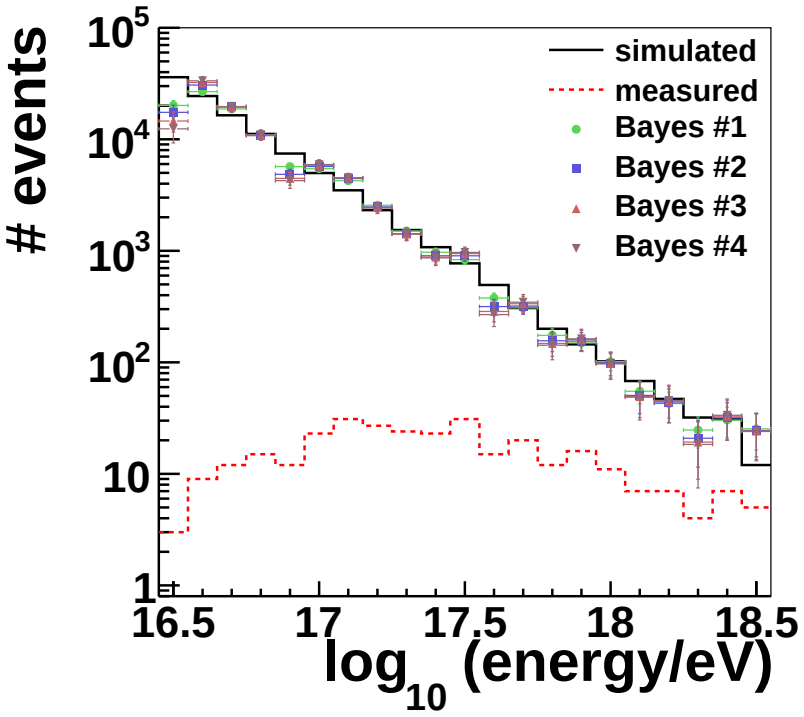

(a)

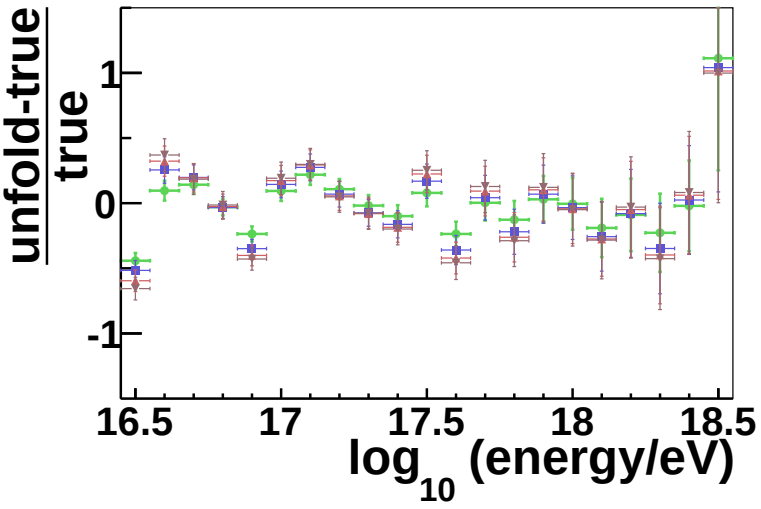

(b)

Figure 6.8: Results of Bayes unfolding for one to four iterations. QGSJETII-04, primary H.

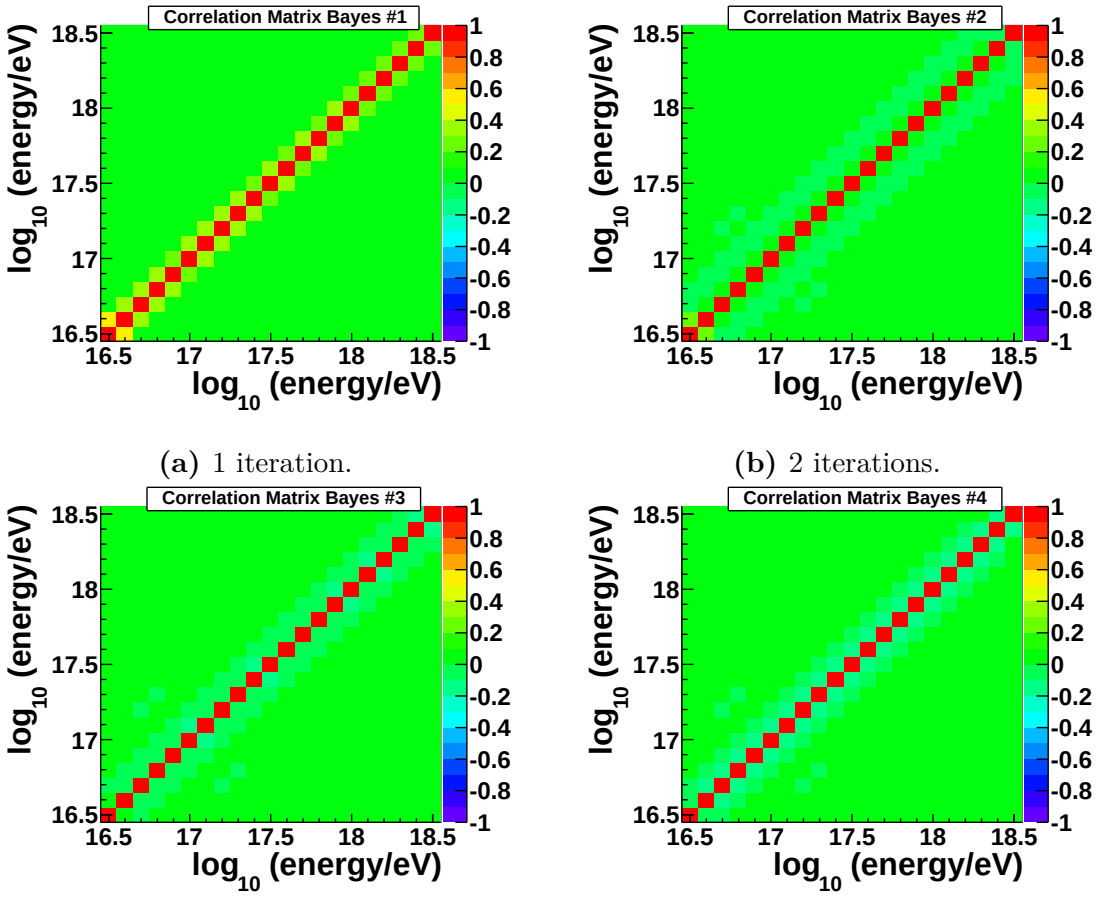

(a) 1 iteration.

(b) 2 iterations.

(c) 3 iterations.

(d) 4 iterations.

Figure 6.9: Correlation matrices for unfolding with Bayes Unfolding. QGSJETII-04, primary H.

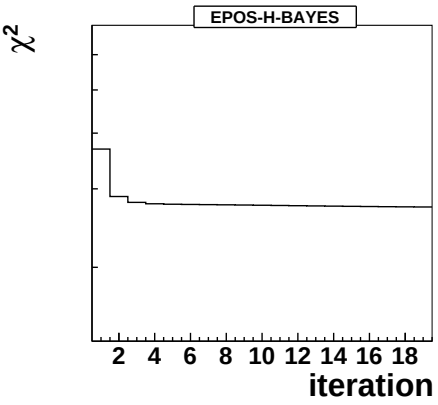

(a) χ^2 test results.

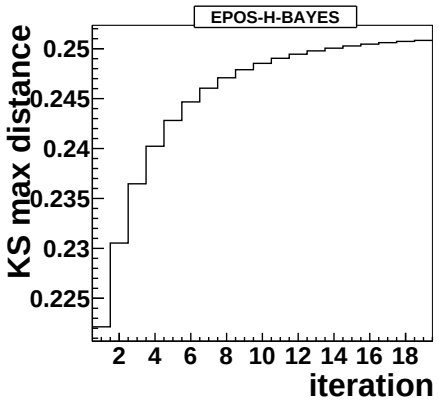

(b) K-S test results.

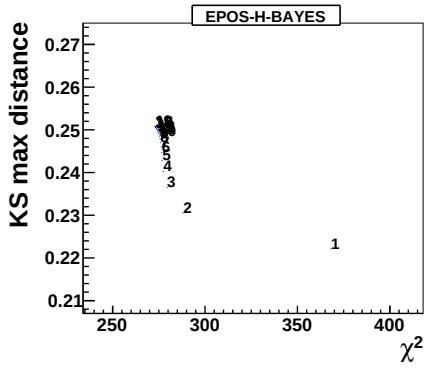

(c) L-Curve.

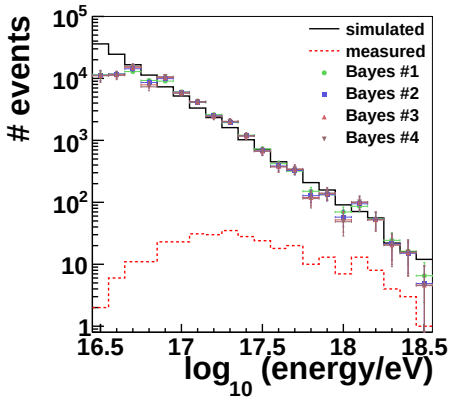

(d) Results of Bayes unfolding for one to four iterations.

Figure 6.10: Results for the unfolding of the test distribution with Bayes Unfolding. EPOS LHC, primary H.

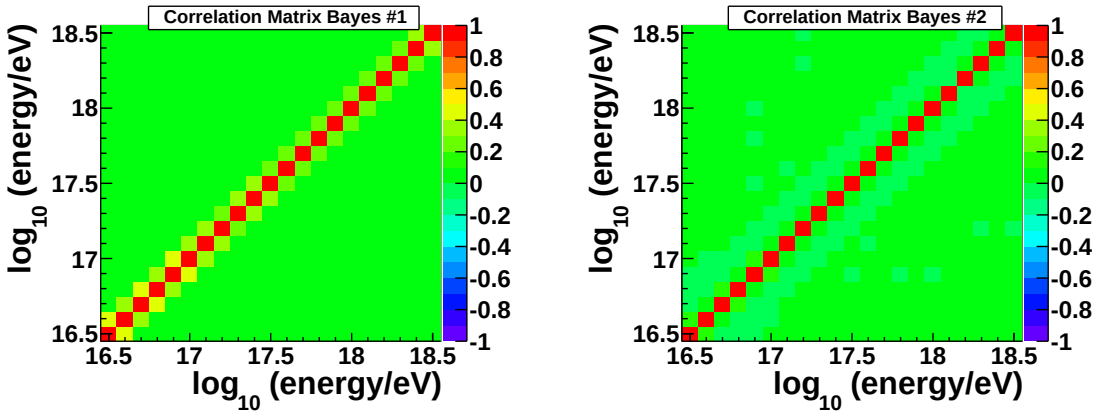

(a) 1 iteration.

(b) 2 iterations.

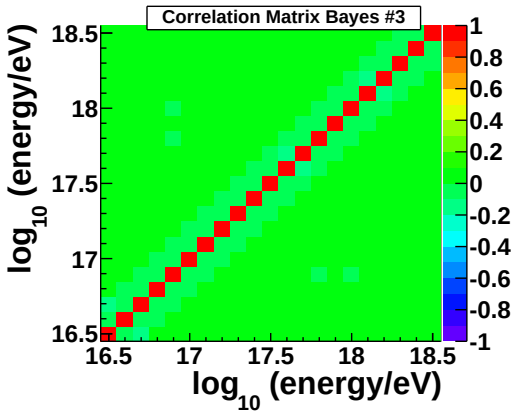

(c) 3 iterations.

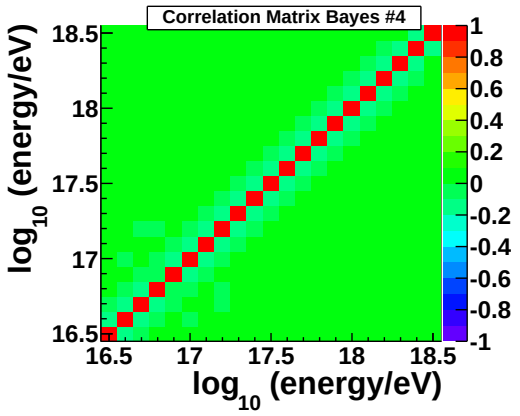

(d) 4 iterations.

Figure 6.11: Correlation matrices for unfolding with Bayes Unfolding. EPOS-LHC, primary H.

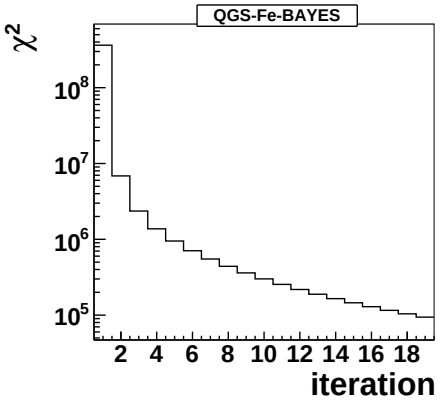

(a) χ^2 test results. QGSJETII-04.

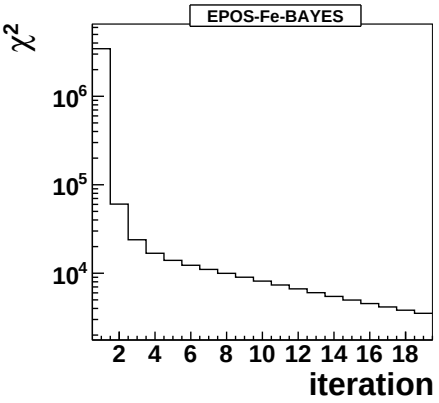

(b) χ^2 test results. EPOS-LHC.

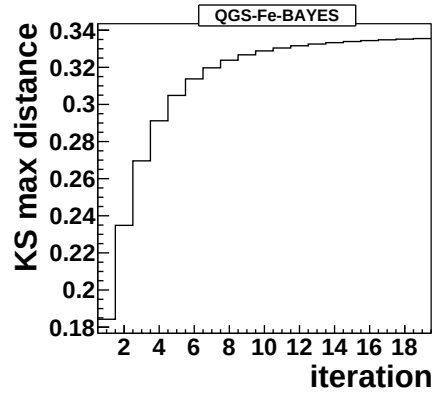

(c) K-S test results. QGSJETII-04.

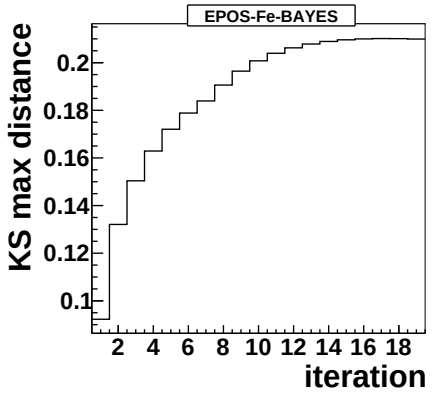

(d) K-S test results. EPOS-LHC.

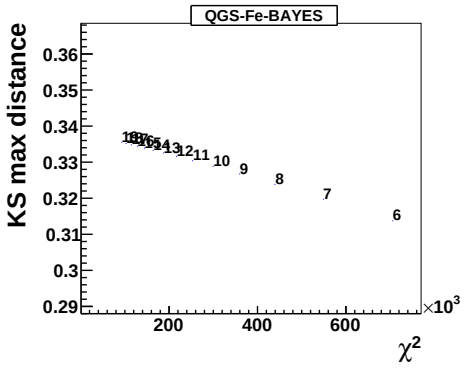

(e) L-Curve. QGSJETII-04.

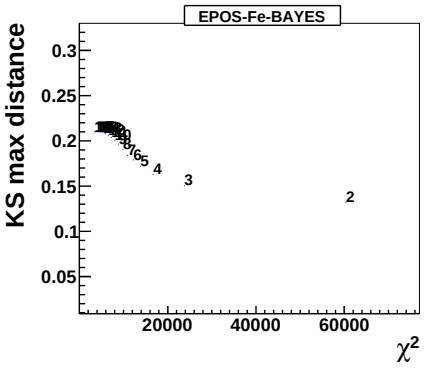

(f) L-Curve. EPOS-LHC.

Figure 6.12: Results for the unfolding of the test distribution with Bayes Unfolding. QGSJETII-04 on the left hand side. EPOS-LHC on the right hand side. Both primary Fe.

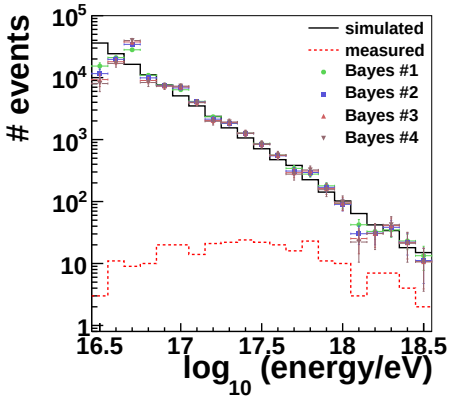

(a) Results of the unfolding. QGSJETII-04.

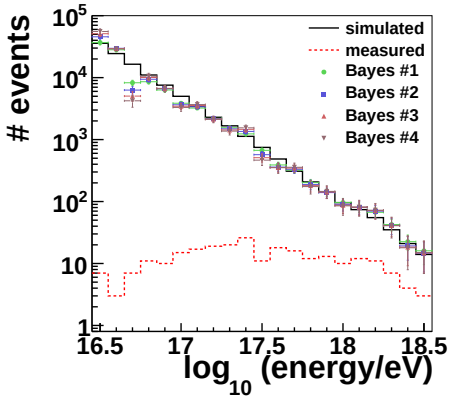

(b) Results of the unfolding. EPOS-LHC.

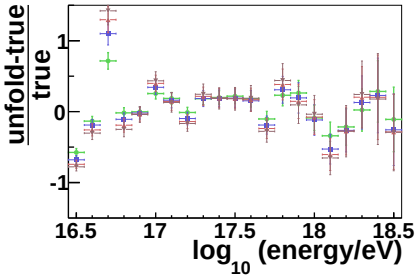

(c) Difference between unfolded and simulated data. QGSJETII-04.

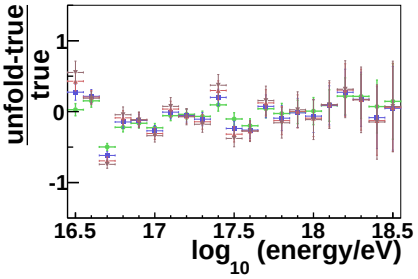

(d) Difference between unfolded and simulated data. EPOS-LHC.

Figure 6.13: Lowest number of iteration results of unfolding with Bayes Unfolding. QGSJETII-04 on the left hand side. EPOS-LHC on the right hand side. Both primary Fe.

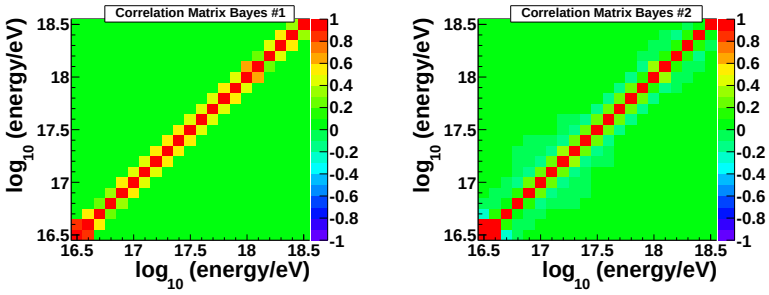

(a) 1 iteration.

(b) 2 iterations.

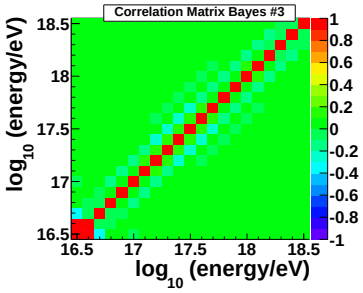

(c) 3 iterations.

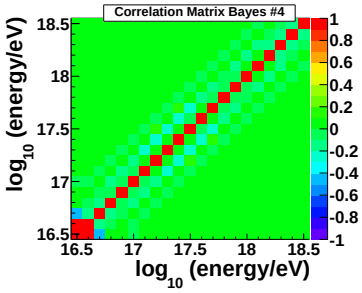

(d) 4 iterations.

Figure 6.14: Correlation matrices for unfolding with Bayes Unfolding. QGSJETII-04, primary Fe.

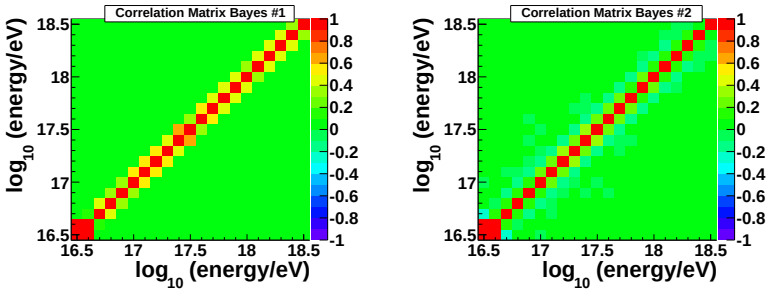

(a) 1 iteration.

(b) 2 iterations.

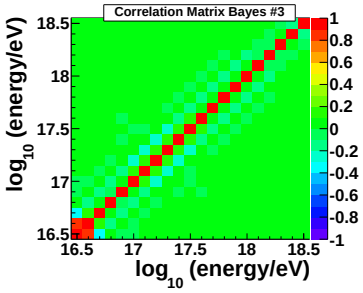

(c) 3 iterations.

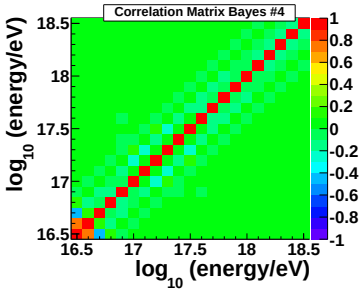

(d) 4 iterations.

Figure 6.15: Correlation matrices for unfolding with Bayes Unfolding. EPOS-LHC, primary Fe.

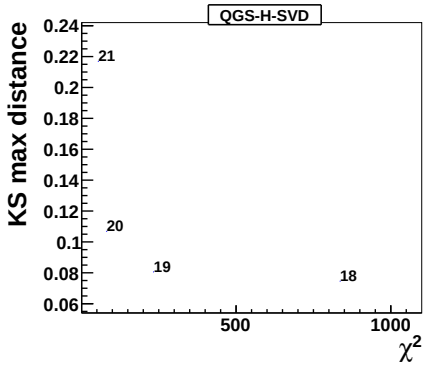

(a) L curve, QGSJETII-04, primary H.

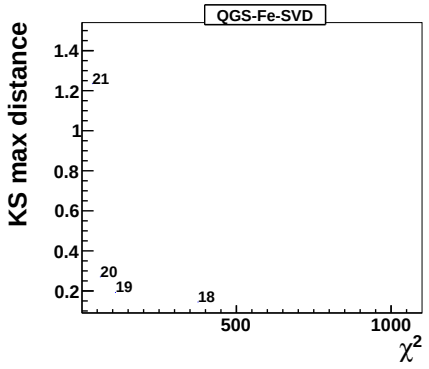

(b) L curve, QGSJETII-04, primary Fe.

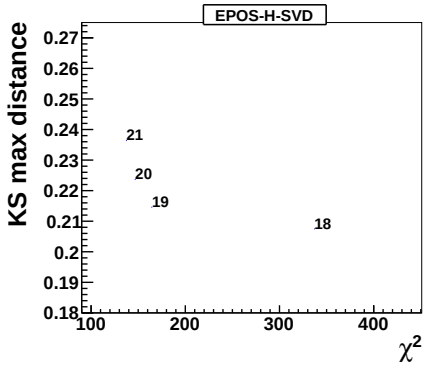

(c) L curve, EPOS-LHC, primary H.

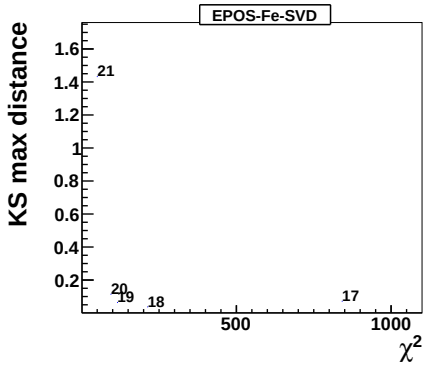

(d) L curve, EPOS-LHC, primary Fe.

Figure 6.16: Results for the unfolding of the test distribution with SVD Unfolding.

6.2.2 SVD Unfolding

To test the unfolding based on Singular Value Decomposition, the unfolding was applied to the test MC sample for multiple regularization parameters (k). As described before, the χ^2 test and the K-S test are performed for every single data set and plotted against each other in an L-curve plot. These plots are given in 6.16. All L-curves show a good behaviour and provide k = 19 as a good choice. The relevant results (k=17...20) are given in fig. 6.17.

Fig. 6.18 present the correlation matrices corresponding to the data given in fig. 6.17b. Furthermore, an example for an overregularized unfolding is given in 6.18e. Positive correlation dominate large parts of the correlation matrix. In the opposite case, the underregularized unfolding, (fig. 6.18d) oscillations between positive and negative correlated bins can be observed along the diagonal. The unfolded distribution of these cases are shown in fig. 6.19a and 6.19b. In case of overregularization the low energy bins show a systematic to be underestimated. The data obtained by the underregularized unfolding oscillates rapidly, as expected.

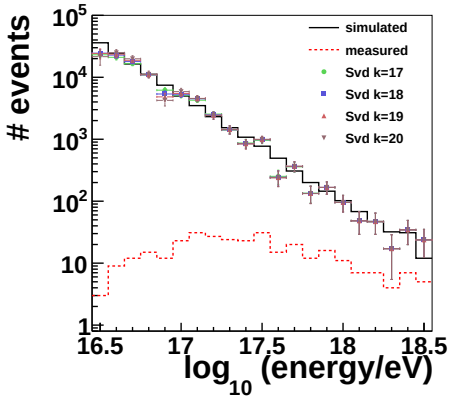

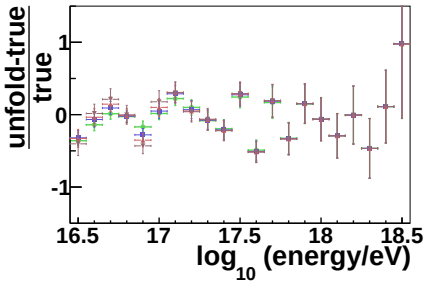

(a) QGSJETII-04, primary H.

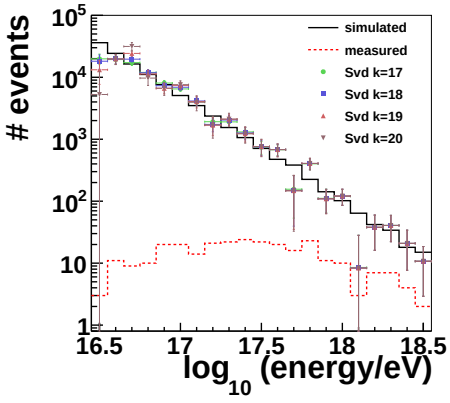

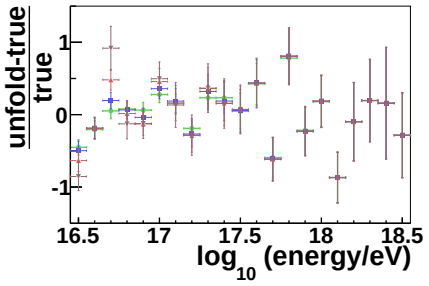

(b) QGSJETII-04, primary Fe.

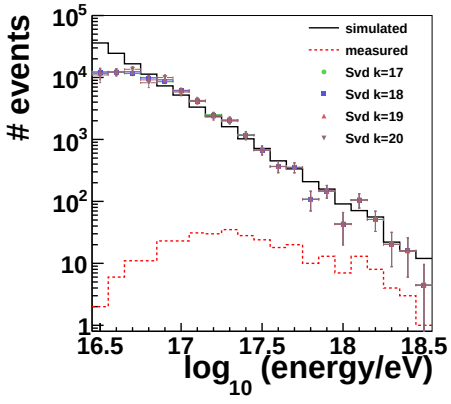

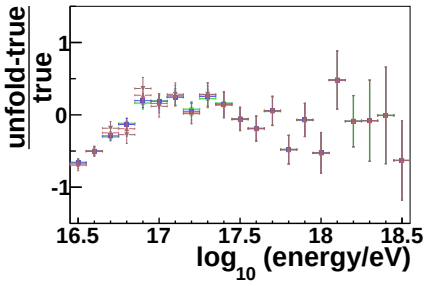

(c) EPOS-LHC, primary H.

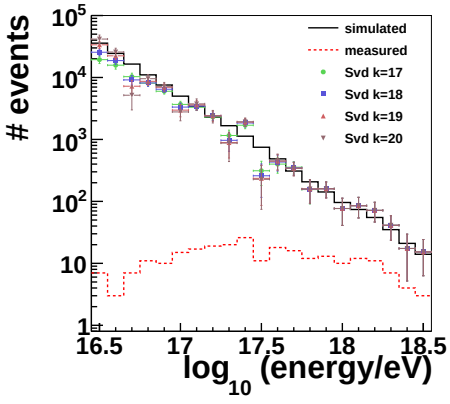

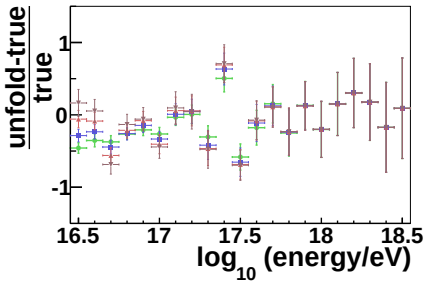

(d) EPOS-LHC, primary Fe.

Figure 6.17: Results for the unfolding of the test distribution with SVD Unfolding. k = 17...20.

Model Primary	QGSJETII-04	EPOS-LHC
H	19	19
Fe	19	19

Table 2: Regularization parameters for SVD.

The chosen regularization parameters for the real data unfolding are given in table 2.

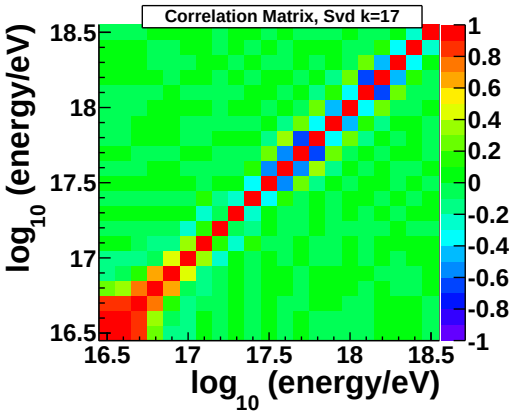

(a) k=17.

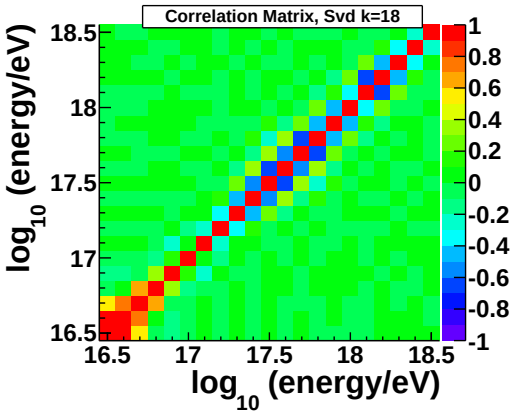

(b) k=18.

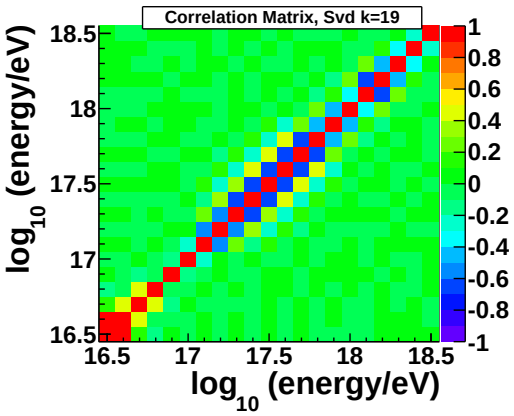

(c) k=19.

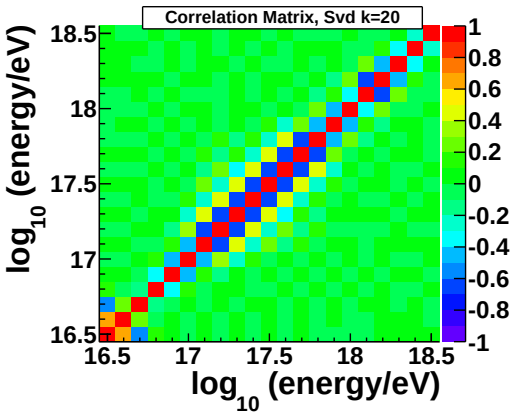

(d) k=20.

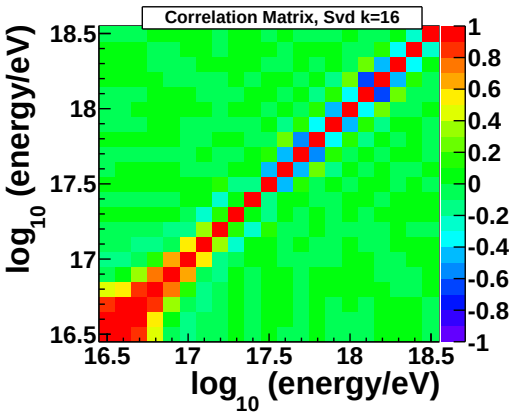

(e) Example for overregularized unfolding, k=16.

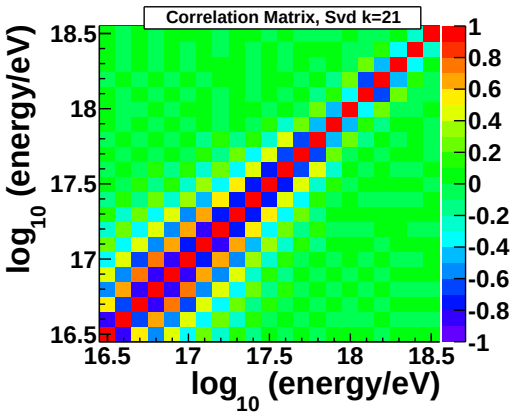

(f) Example for underregularized unfolding, k=21.

Figure 6.18: Correlation matrices for unfolding with SVD Unfolding. QGSJETII-04, primary Fe.

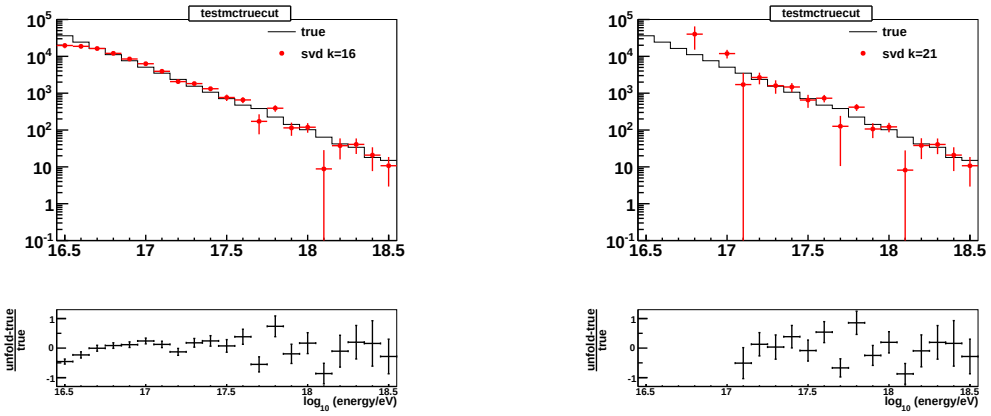

(a) Example for overregularized unfolding, k=16.

(b) Example for underregularized unfolding, k=21.

Figure 6.19: Examples for under-/overregularized unfolding with SVD Unfolding. QGSJETII-04, primary Fe.

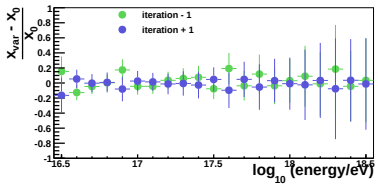

(a) QGSJETII-04, primary H.

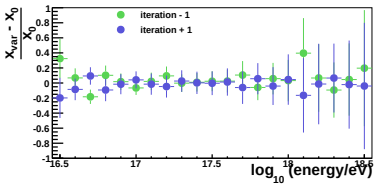

(b) QGSJETII-04, primary Fe.

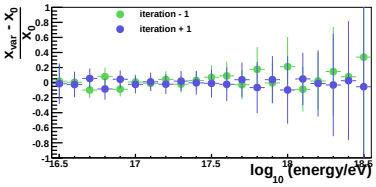

(c) EPOS-LHC, primary H.

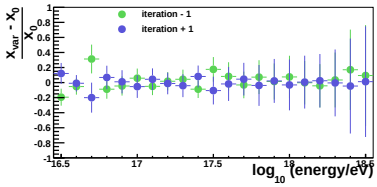

(d) EPOS-LHC, primary Fe.

Figure 6.20: Estimating the systematic errors from the choice of regularisation parameter with Bayes unfolding.

6.3 Systematic uncertainties

The systematic uncertainties on the FD energy reconstruction can be summarized to 22%. [38] (A detailed discussion of the individual contributions can be found in this source.)

Furthermore, systematic uncertainties arise from the choice of the regularisation parameter and the interaction model as well as the primary particle.

Regularisation parameter

To probe the influence of the choice of the regularisation parameter, the regularisation parameter is varied by ± 1 and the unfolding is performed. Then, the difference between the results of the initial unfolding x_0 and the varied one x_{var} is calculated and normalized to the initial values:

$$\Delta x = \frac{x_{var} - x_0}{x_0}. \tag{6.4}$$

The resulting plots are given in fig. 6.20 and 6.21 for each combination of interaction model and primary particle. The mean errors are given in table 3 and 4. They are all clearly smaller than 2%.

Interaction model and primary particle

In order to estimate the systematic uncertainty due to the different interaction models and choice of primary particle, the unfolding was performed with varying constellations. For example, in fig. 6.22a the test for Bayes Unfolding with interaction model QGSJETII-04 and primary particle H is shown. The given distributions are calculated as before (eq. 6.4). Here, x_0 corresponds to the standard unfolding of

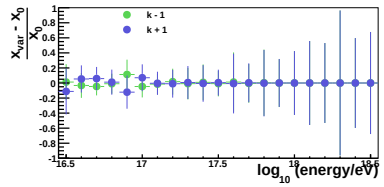

(a) QGSJETII-04, primary H.

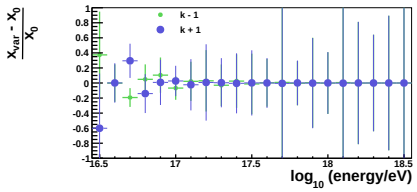

(b) QGSJETII-04, primary Fe.

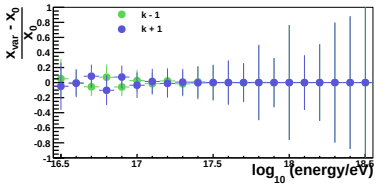

(c) EPOS-LHC, primary H.

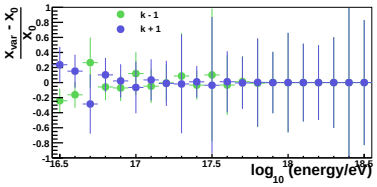

(d) EPOS-LHC, primary Fe.

Figure 6.21: Estimating the systematic errors from the choice of regularisation parameter with SVD unfolding.

Model / Primary	QGSJETII-04	EPOS-LHC
H	1.2%	1.3%
Fe	1.7%	1.4%

Table 3: Systematic uncertainties for Bayes Unfolding from the choice of the regularisation parameter.

the QGSJETII-04, H test sample with the QGSJETII-04, H response matrix. x_{var} is calculated by unfolding the other three data samples (QGSJETII-04, Fe; EPOS-LHC, H; EPOS-LHC, Fe) with the same response matrix as for x_0. Some examples are shown in 6.22.

The average systematic uncertainty for all possible combinations of interaction models and primary particles was conservatively estimated to 15%.

All three uncertainties are summed up and given in table 5 and 6. They are highly

Model / Primary	QGSJETII-04	EPOS-LHC
H	0.6%	0.5%
Fe	1.9%	1.5%

Table 4: Systematic uncertainties for SVD Unfolding from the choice of the regularisation parameter.

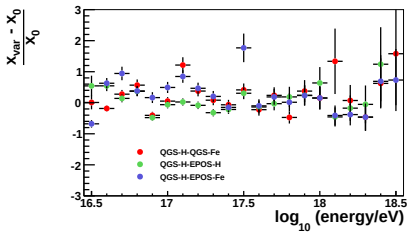

(a) QGSJETII-04, primary H, Bayes Unfolding. $\sigma_{sys} = 9.5\%$.

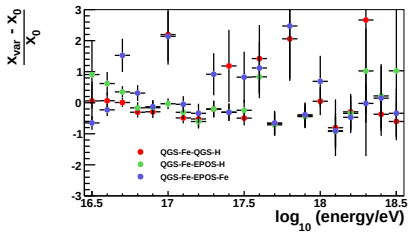

(b) QGSJETII-04, primary Fe, SVD Unfolding. $\sigma_{sys} = 14.1\%$.

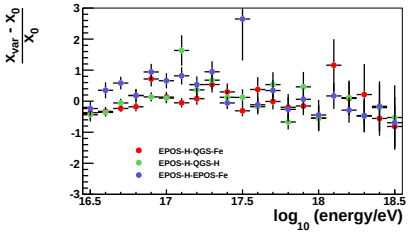

(c) EPOS-LHC, primary H, SVD Unfolding. $\sigma_{sys} = 14.0\%$.

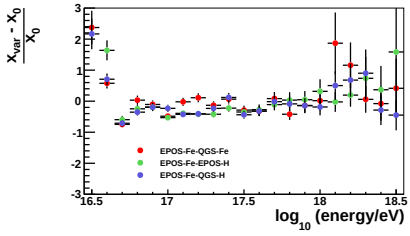

(d) EPOS-LHC, primary Fe, Bayes Unfolding. $\sigma_{sys} = 10.3\%$.

Figure 6.22: Estimating the systematic errors from the different interaction models and primary particles.

Model / Primary	QGSJETII-04	EPOS-LHC
H	26.65%	26.66%
Fe	26.68%	26.66%

Table 5: Systematic uncertainties for Bayes Unfolding.

dominated by the energy reconstruction.

Model / Primary	QGSJETII-04	EPOS-LHC
H	26.63%	26.63%
Fe	26.69%	26.67%

Table 6: Systematic uncertainties for SVD Unfolding.

6.4 Apply Unfolding to Auger data

To calculate the flux of cosmic rays from the unfolded number of events one has to take into account the exposure ($\epsilon(E)$) of the detector. This calculation is described in [39] and will be introduced briefly. With $\Delta N_{unf}(E)$ being the number of unfolded events in an energy bin E with the width ΔE, the flux $J(E)$ can be written as

$$J(E) = \frac{\Delta N_{unf}(E)}{\Delta E \cdot \epsilon(E)}. \tag{6.5}$$

The exposure $\epsilon(E)$ is given by

$$\epsilon(E) = \int_T A(E,t)\mathrm{d}t, \tag{6.6}$$

with the aperture $A(E,T) = \int_\Omega S_{\text{eff}}\mathrm{d}\Omega$. As the data for this analysis was taken with a time-independent detector configuration the uptime calculation can be decoupled from the aperture calculation. The uptime calculation for the time period from June 2010 (2010-05-31 T23:09:58Z) till August 2011 (2011-09-13 T12:49:58Z) for the HEAT telescopes was performed in [25] and yield 2640000 ± 40000 seconds.

The effective area $S_{\text{eff}} = e(E) \times S_{\text{gen}}$ depends on the efficiency $e(E)$ of the detector and the generation area S_{gen} for the dataset. The aperture can be calculated as follows:

$$A(E) = \int_\Omega S_{\text{eff}}\mathrm{d}\Omega = \pi(1 - \cos^2\theta_{\max})S_{\text{eff}} \tag{6.7}$$

After carrying out the space angle integration and with a maximum zenith angle of $\theta_{\max} = 60°$ the aperture reads:

$$A(E) = \frac{3}{4}\pi \text{ sr} \times S_{\text{eff}}. \tag{6.8}$$

Finally, the generated area has to be calculated. This area is described by a circle segment of 180°, an inner radius of 1000 m and an energy dependent outer radius that reaches from 6000 to 40500 m. The effective area in dependence of the energy is given in fig. 6.23.

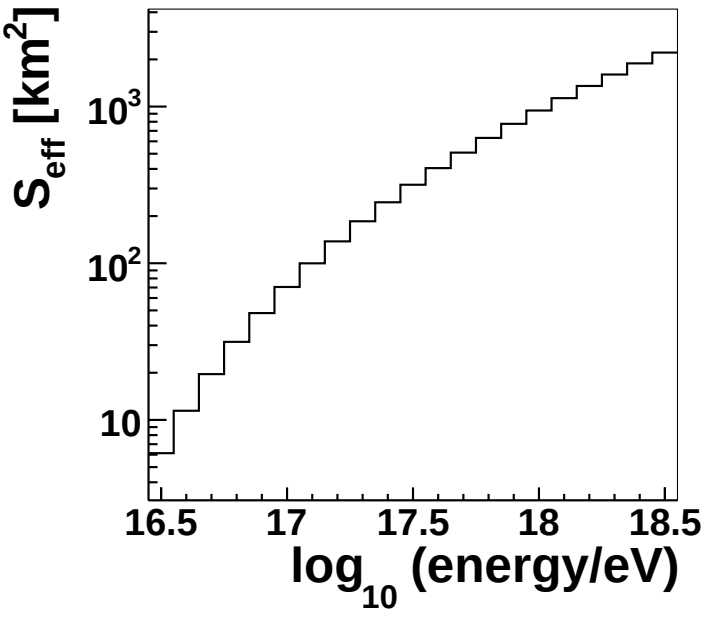

Figure 6.23: Effective area S_{eff}.

Energy in $log_{10}E/eV$	Effective area $S_{\text{eff}}[km^2]$
16.5	6.13
16.6	11.44
16.7	19.60
16.8	31.49
16.9	48.07
17.0	70.54
17.1	99.88
17.2	137.90
17.3	185.30
17.4	244.95
17.5	316.95
17.6	404.70
17.7	508.24
17.8	630.85
17.9	775.90
18.0	943.67
18.1	1131.81
18.2	1353.67
18.3	1601.72
18.4	1886.63
18.5	2210.75

Table 7: Effective area S_{eff}.

Energy in $log_{10}E/eV$	Number of reconstructed events
16.5	70
16.6	165
16.7	310
16.8	551
16.9	842
17.0	1169
17.1	1485
17.2	1933
17.3	2129
17.4	2209
17.5	2137
17.6	1965
17.7	1690
17.8	1282
17.9	1014
18.0	759
18.1	526
18.2	365
18.3	280
18.4	179
18.5	112

Table 8: Number of reconstructed events.

6.4.1 Results

The number of reconstructed events in the mentioned period of time with the HEAT detector is given in table 8 and shown in fig. 6.24.

Now the flux can be calculated for each data set. The results are given in the tables 9-16. The corresponding plots are shown in fig. 6.25a-6.32a. Systematic uncertainties are drawn as a green band, while the statistic uncertainties are represented by the error bars. Furthermore, the correlation matrices are given for each distribution in fig. 6.25b-6.32b.

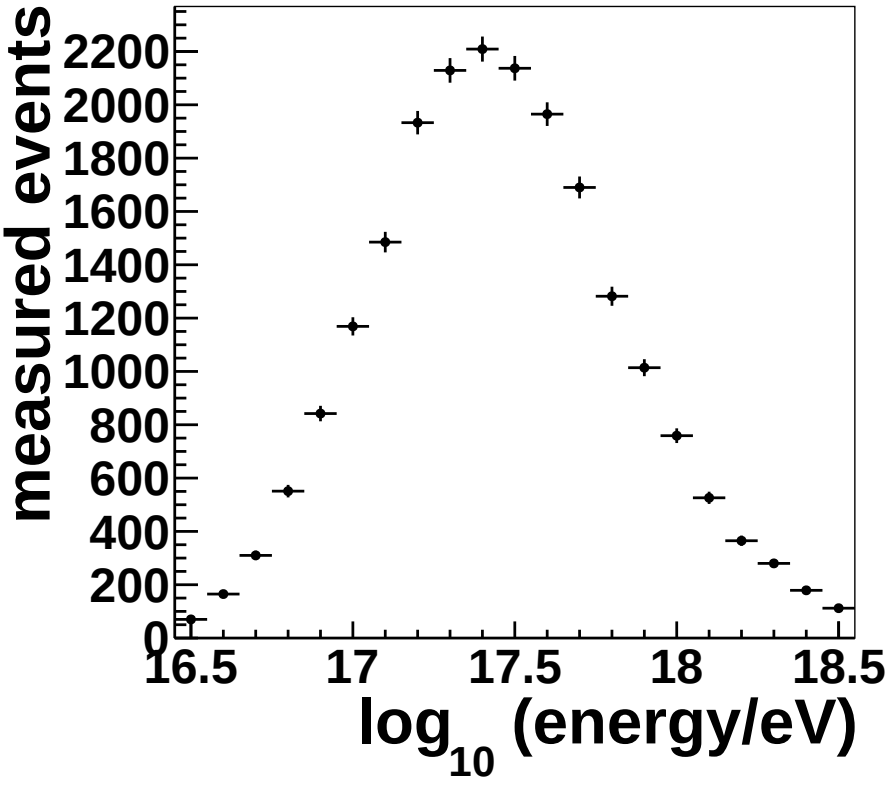

Figure 6.24: Measured events during the time period of June 2010 to August 2011 with HEAT.

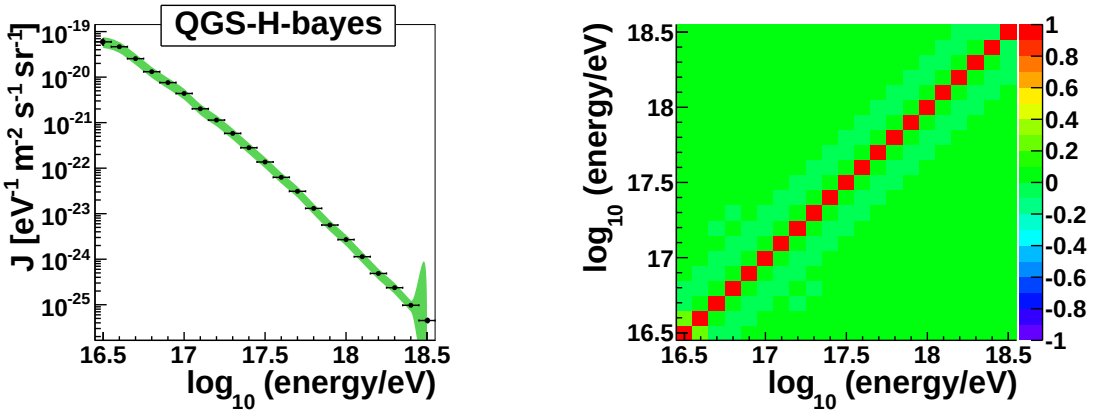

(a) Unfolded flux $J[eV^{-1}m^{-2}s^{-1}sr^{-1}]$.

(b) Correlation matrix.

Figure 6.25: QGSJETII-04, H, Bayes Unfolding

Energy in $log_{10}E/eV$	$J[eV^{-1}m^{-2}s^{-1}sr^{-1}]$
16.5	$5.94876 \cdot 10^{-20} \pm 9.06954 \cdot 10^{-21}$
16.6	$4.64932 \cdot 10^{-20} \pm 3.70844 \cdot 10^{-21}$
16.7	$2.54697 \cdot 10^{-20} \pm 1.50556 \cdot 10^{-21}$
16.8	$1.31503 \cdot 10^{-20} \pm 6.25338 \cdot 10^{-22}$
16.9	$7.58175 \cdot 10^{-21} \pm 3.01018 \cdot 10^{-22}$
17.0	$4.37453 \cdot 10^{-21} \pm 1.48412 \cdot 10^{-22}$
17.1	$2.01627 \cdot 10^{-21} \pm 6.182 \cdot 10^{-23}$
17.2	$1.1377 \cdot 10^{-21} \pm 3.15838 \cdot 10^{-23}$
17.3	$5.80752 \cdot 10^{-22} \pm 1.56225 \cdot 10^{-23}$
17.4	$2.81155 \cdot 10^{-22} \pm 7.44452 \cdot 10^{-24}$
17.5	$1.36663 \cdot 10^{-22} \pm 3.67689 \cdot 10^{-24}$
17.6	$6.29006 \cdot 10^{-23} \pm 1.73943 \cdot 10^{-24}$
17.7	$3.10334 \cdot 10^{-23} \pm 9.02662 \cdot 10^{-25}$
17.8	$1.30752 \cdot 10^{-23} \pm 4.1936 \cdot 10^{-25}$
17.9	$5.63098 \cdot 10^{-24} \pm 2.01322 \cdot 10^{-25}$
18.0	$2.69435 \cdot 10^{-24} \pm 1.06543 \cdot 10^{-25}$
18.1	$1.13607 \cdot 10^{-24} \pm 5.3336 \cdot 10^{-26}$
18.2	$4.86614 \cdot 10^{-25} \pm 2.71991 \cdot 10^{-26}$
18.3	$2.36653 \cdot 10^{-25} \pm 1.47402 \cdot 10^{-26}$
18.4	$9.73344 \cdot 10^{-26} \pm 7.53858 \cdot 10^{-27}$
18.5	$4.50145 \cdot 10^{-26} \pm 4.26148 \cdot 10^{-27}$

Table 9: Unfolded flux, QGSJETII-04, primary H, Bayes Unfolding.

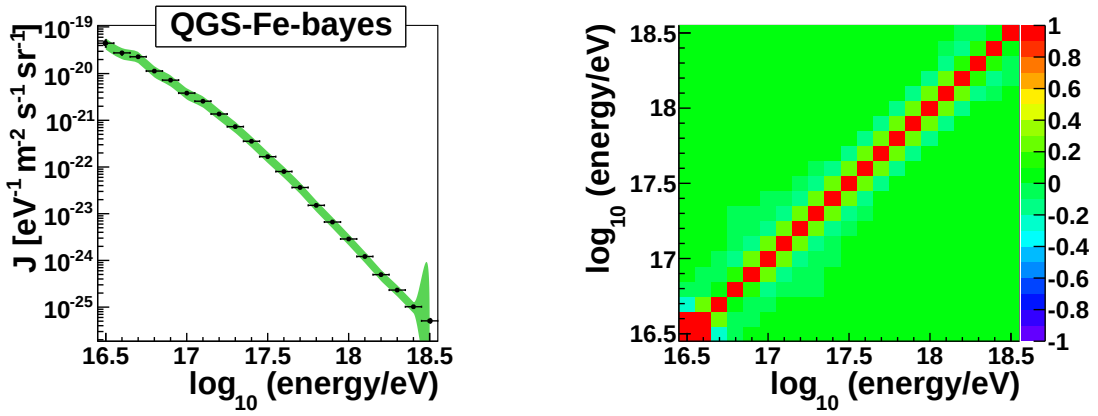

(a) Unfolded flux $J[eV^{-1}m^{-2}s^{-1}sr^{-1}]$. **(b)** Correlation matrix.

Figure 6.26: QGSJETII-04, Fe, Bayes Unfolding

Energy in $log_{10}E/eV$	$J[eV^{-1}m^{-2}s^{-1}sr^{-1}]$
16.5	$6.12748 \cdot 10^{-20} \pm 2.24758 \cdot 10^{-20}$
16.6	$4.23606 \cdot 10^{-20} \pm 5.45208 \cdot 10^{-21}$
16.7	$2.50906 \cdot 10^{-20} \pm 2.57142 \cdot 10^{-21}$
16.8	$1.33033 \cdot 10^{-20} \pm 1.22734 \cdot 10^{-21}$
16.9	$7.62523 \cdot 10^{-21} \pm 5.89529 \cdot 10^{-22}$
17.0	$4.33764 \cdot 10^{-21} \pm 2.93797 \cdot 10^{-22}$
17.1	$2.01459 \cdot 10^{-21} \pm 1.316 \cdot 10^{-22}$
17.2	$1.13779 \cdot 10^{-21} \pm 6.48336 \cdot 10^{-23}$
17.3	$5.8343 \cdot 10^{-22} \pm 3.24001 \cdot 10^{-23}$
17.4	$2.79219 \cdot 10^{-22} \pm 1.42985 \cdot 10^{-23}$
17.5	$1.37733 \cdot 10^{-22} \pm 6.55592 \cdot 10^{-24}$
17.6	$6.21978 \cdot 10^{-23} \pm 3.09076 \cdot 10^{-24}$
17.7	$3.14898 \cdot 10^{-23} \pm 1.54474 \cdot 10^{-24}$
17.8	$1.29356 \cdot 10^{-23} \pm 6.49772 \cdot 10^{-25}$
17.9	$5.62705 \cdot 10^{-24} \pm 2.94271 \cdot 10^{-25}$
18.0	$2.69858 \cdot 10^{-24} \pm 1.49836 \cdot 10^{-25}$
18.1	$1.14151 \cdot 10^{-24} \pm 6.87873 \cdot 10^{-26}$
18.2	$4.78379 \cdot 10^{-25} \pm 3.54262 \cdot 10^{-26}$
18.3	$2.41602 \cdot 10^{-25} \pm 1.82264 \cdot 10^{-26}$
18.4	$9.62708 \cdot 10^{-26} \pm 9.5447 \cdot 10^{-27}$
18.5	$4.47474 \cdot 10^{-26} \pm 4.8729 \cdot 10^{-27}$

Table 10: Unfolded flux, QGSJETII-04, primary H, SVD Unfolding.

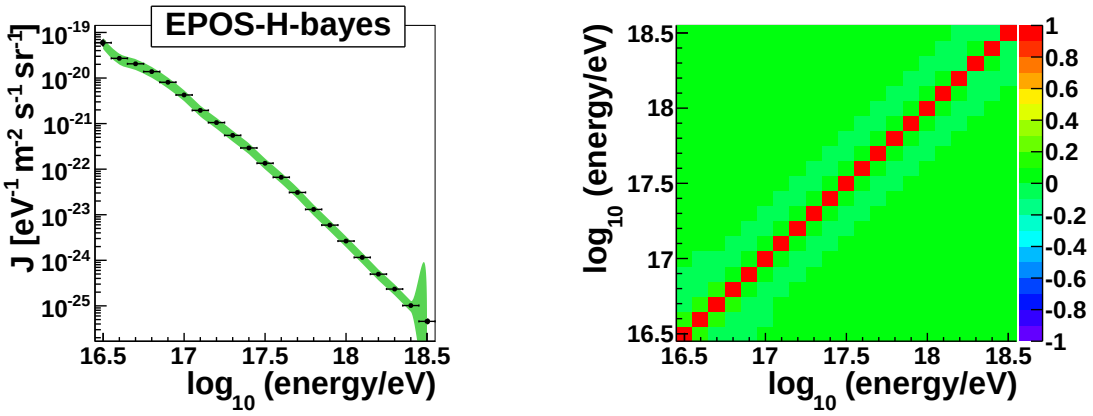

(a) Unfolded flux $J[eV^{-1}m^{-2}s^{-1}sr^{-1}]$. **(b)** Correlation matrix.

Figure 6.27: EPOS-LHC, H, Bayes Unfolding

Energy in $log_{10}E/eV$	$J[eV^{-1}m^{-2}s^{-1}sr^{-1}]$
16.5	$4.47662 \cdot 10^{-20} \pm 7.81872 \cdot 10^{-21}$
16.6	$2.77589 \cdot 10^{-20} \pm 2.76067 \cdot 10^{-21}$
16.7	$2.29326 \cdot 10^{-20} \pm 1.74291 \cdot 10^{-21}$
16.8	$1.13351 \cdot 10^{-20} \pm 6.24477 \cdot 10^{-22}$
16.9	$7.24209 \cdot 10^{-21} \pm 2.89666 \cdot 10^{-22}$
17.0	$3.81968 \cdot 10^{-21} \pm 1.26885 \cdot 10^{-22}$
17.1	$2.56273 \cdot 10^{-21} \pm 7.69887 \cdot 10^{-23}$
17.2	$1.3648 \cdot 10^{-21} \pm 3.57241 \cdot 10^{-23}$
17.3	$7.31235 \cdot 10^{-22} \pm 1.8004 \cdot 10^{-23}$
17.4	$3.55819 \cdot 10^{-22} \pm 8.57268 \cdot 10^{-24}$
17.5	$1.66414 \cdot 10^{-22} \pm 4.00685 \cdot 10^{-24}$
17.6	$8.00689 \cdot 10^{-23} \pm 1.98326 \cdot 10^{-24}$
17.7	$3.64086 \cdot 10^{-23} \pm 9.44869 \cdot 10^{-25}$
17.8	$1.50975 \cdot 10^{-23} \pm 4.24002 \cdot 10^{-25}$
17.9	$6.63785 \cdot 10^{-24} \pm 2.09295 \cdot 10^{-25}$
18.0	$2.87655 \cdot 10^{-24} \pm 1.01433 \cdot 10^{-25}$
18.1	$1.21306 \cdot 10^{-24} \pm 4.9651 \cdot 10^{-26}$
18.2	$4.9542 \cdot 10^{-25} \pm 2.39989 \cdot 10^{-26}$
18.3	$2.31717 \cdot 10^{-25} \pm 1.2954 \cdot 10^{-26}$
18.4	$1.01863 \cdot 10^{-25} \pm 6.88776 \cdot 10^{-27}$
18.5	$5.07821 \cdot 10^{-26} \pm 4.22982 \cdot 10^{-27}$

Table 11: Unfolded flux, QGSJETII-04, primary Fe, Bayes Unfolding.

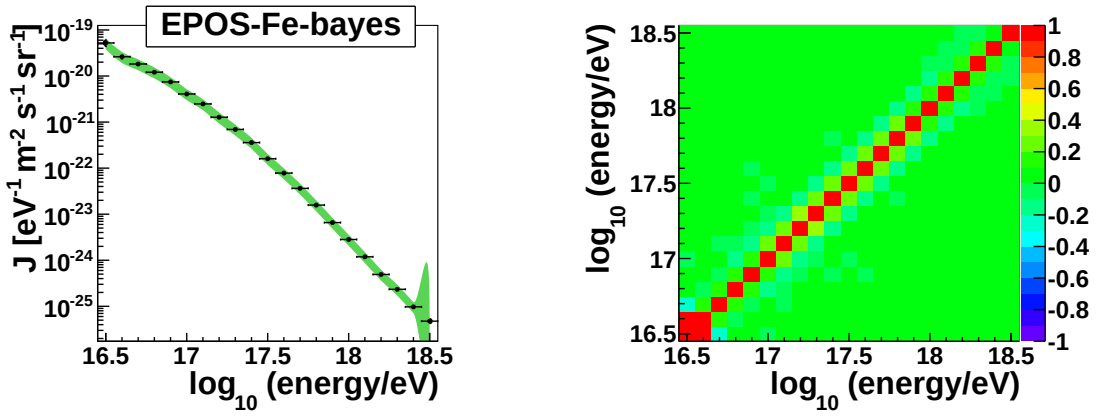

(a) Unfolded flux $J[eV^{-1}m^{-2}s^{-1}sr^{-1}]$. **(b)** Correlation matrix.

Figure 6.28: EPOS-LHC, Fe, Bayes Unfolding

Energy in $log_{10}E/eV$	$J[eV^{-1}m^{-2}s^{-1}sr^{-1}]$
16.5	$2.44182 \cdot 10^{-20} \pm 2.32843 \cdot 10^{-20}$
16.6	$2.82099 \cdot 10^{-20} \pm 5.33619 \cdot 10^{-21}$
16.7	$2.28299 \cdot 10^{-20} \pm 3.2997 \cdot 10^{-21}$
16.8	$1.11233 \cdot 10^{-20} \pm 1.46353 \cdot 10^{-21}$
16.9	$7.39915 \cdot 10^{-21} \pm 7.16745 \cdot 10^{-22}$
17.0	$3.58997 \cdot 10^{-21} \pm 3.58178 \cdot 10^{-22}$
17.1	$2.67496 \cdot 10^{-21} \pm 2.22315 \cdot 10^{-22}$
17.2	$1.33741 \cdot 10^{-21} \pm 1.06447 \cdot 10^{-22}$
17.3	$7.41851 \cdot 10^{-22} \pm 5.59657 \cdot 10^{-23}$
17.4	$3.5734 \cdot 10^{-22} \pm 2.74365 \cdot 10^{-23}$
17.5	$1.63755 \cdot 10^{-22} \pm 1.2304 \cdot 10^{-23}$
17.6	$7.97851 \cdot 10^{-23} \pm 5.37759 \cdot 10^{-24}$
17.7	$3.7852 \cdot 10^{-23} \pm 2.45886 \cdot 10^{-24}$
17.8	$1.42937 \cdot 10^{-23} \pm 9.84046 \cdot 10^{-25}$
17.9	$6.86495 \cdot 10^{-24} \pm 4.28969 \cdot 10^{-25}$
18.0	$2.82137 \cdot 10^{-24} \pm 1.97495 \cdot 10^{-25}$
18.1	$1.24262 \cdot 10^{-24} \pm 9.12103 \cdot 10^{-26}$
18.2	$4.71845 \cdot 10^{-25} \pm 4.24394 \cdot 10^{-26}$
18.3	$2.44539 \cdot 10^{-25} \pm 2.2271 \cdot 10^{-26}$
18.4	$9.78916 \cdot 10^{-26} \pm 1.15196 \cdot 10^{-26}$
18.5	$5.10688 \cdot 10^{-26} \pm 5.31874 \cdot 10^{-27}$

Table 12: Unfolded flux, QGSJETII-04, primary Fe, SVD Unfolding.

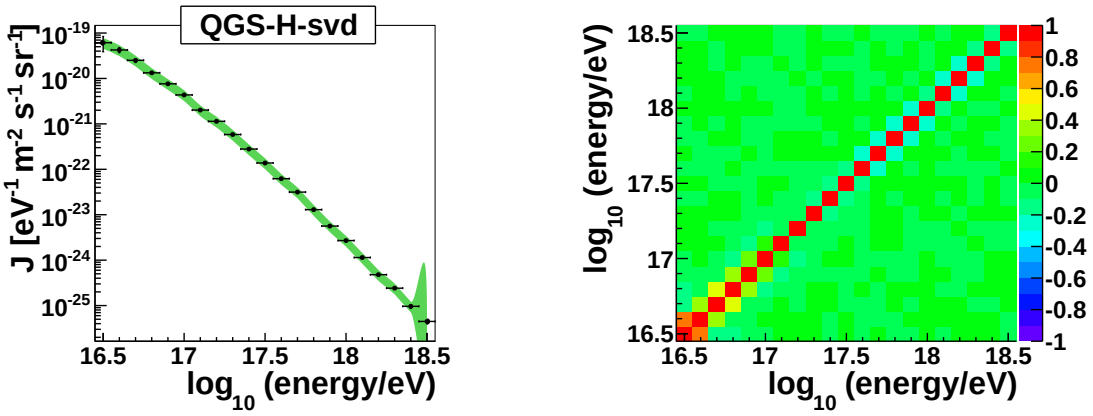

(a) Unfolded flux $J[eV^{-1}m^{-2}s^{-1}sr^{-1}]$. **(b)** Correlation matrix.

Figure 6.29: QGSJETII-04, H, SVD Unfolding

Energy in $log_{10}E/eV$	$J[eV^{-1}m^{-2}s^{-1}sr^{-1}]$
16.5	$5.94632 \cdot 10^{-20} \pm 8.30015 \cdot 10^{-21}$
16.6	$2.70371 \cdot 10^{-20} \pm 2.331 \cdot 10^{-21}$
16.7	$2.0521 \cdot 10^{-20} \pm 1.20163 \cdot 10^{-21}$
16.8	$1.3829 \cdot 10^{-20} \pm 6.38712 \cdot 10^{-22}$
16.9	$8.07647 \cdot 10^{-21} \pm 3.0759 \cdot 10^{-22}$
17.0	$4.24932 \cdot 10^{-21} \pm 1.37896 \cdot 10^{-22}$
17.1	$1.95004 \cdot 10^{-21} \pm 5.95151 \cdot 10^{-23}$
17.2	$1.05315 \cdot 10^{-21} \pm 2.92509 \cdot 10^{-23}$
17.3	$5.51516 \cdot 10^{-22} \pm 1.47615 \cdot 10^{-23}$
17.4	$2.92019 \cdot 10^{-22} \pm 7.63622 \cdot 10^{-24}$
17.5	$1.34878 \cdot 10^{-22} \pm 3.64353 \cdot 10^{-24}$
17.6	$6.62761 \cdot 10^{-23} \pm 1.81689 \cdot 10^{-24}$
17.7	$3.08218 \cdot 10^{-23} \pm 9.04789 \cdot 10^{-25}$
17.8	$1.30782 \cdot 10^{-23} \pm 4.28159 \cdot 10^{-25}$
17.9	$5.91702 \cdot 10^{-24} \pm 2.10702 \cdot 10^{-25}$
18.0	$2.6419 \cdot 10^{-24} \pm 1.06277 \cdot 10^{-25}$
18.1	$1.15583 \cdot 10^{-24} \pm 5.42333 \cdot 10^{-26}$
18.2	$4.96348 \cdot 10^{-25} \pm 2.74834 \cdot 10^{-26}$
18.3	$2.33706 \cdot 10^{-25} \pm 1.50422 \cdot 10^{-26}$
18.4	$1.01592 \cdot 10^{-25} \pm 7.81511 \cdot 10^{-27}$
18.5	$4.56829 \cdot 10^{-26} \pm 4.30015 \cdot 10^{-27}$

Table 13: Unfolded flux, EPOS-LHC, primary H, Bayes Unfolding.

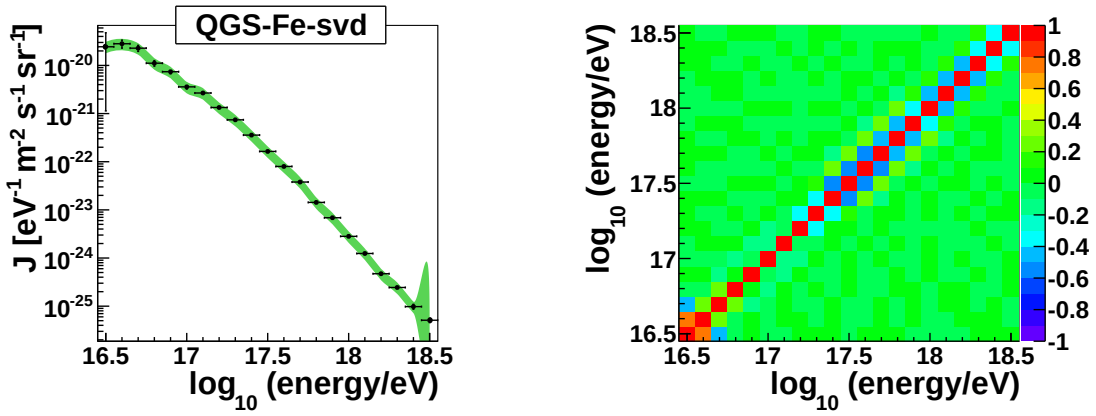

(a) Unfolded flux $J[eV^{-1}m^{-2}s^{-1}sr^{-1}]$. **(b)** Correlation matrix.

Figure 6.30: QGSJETII-04, Fe, SVD Unfolding

Energy in $log_{10}E/eV$	$J[eV^{-1}m^{-2}s^{-1}sr^{-1}]$
16.5	$5.5948 \cdot 10^{-20} \pm 1.30286 \cdot 10^{-20}$
16.6	$2.72234 \cdot 10^{-20} \pm 4.11732 \cdot 10^{-21}$
16.7	$1.99023 \cdot 10^{-20} \pm 2.1696 \cdot 10^{-21}$
16.8	$1.38372 \cdot 10^{-20} \pm 1.17813 \cdot 10^{-21}$
16.9	$8.17818 \cdot 10^{-21} \pm 6.13399 \cdot 10^{-22}$
17.0	$4.23798 \cdot 10^{-21} \pm 2.78234 \cdot 10^{-22}$
17.1	$1.94471 \cdot 10^{-21} \pm 1.26647 \cdot 10^{-22}$
17.2	$1.05272 \cdot 10^{-21} \pm 6.11818 \cdot 10^{-23}$
17.3	$5.4952 \cdot 10^{-22} \pm 3.003 \cdot 10^{-23}$
17.4	$2.96497 \cdot 10^{-22} \pm 1.54835 \cdot 10^{-23}$
17.5	$1.32551 \cdot 10^{-22} \pm 6.89037 \cdot 10^{-24}$
17.6	$6.66541 \cdot 10^{-23} \pm 3.11017 \cdot 10^{-24}$
17.7	$3.08972 \cdot 10^{-23} \pm 1.50895 \cdot 10^{-24}$
17.8	$1.29927 \cdot 10^{-23} \pm 6.56416 \cdot 10^{-25}$
17.9	$5.92728 \cdot 10^{-24} \pm 2.99307 \cdot 10^{-25}$
18.0	$2.64319 \cdot 10^{-24} \pm 1.49899 \cdot 10^{-25}$
18.1	$1.15883 \cdot 10^{-24} \pm 7.27943 \cdot 10^{-26}$
18.2	$4.909 \cdot 10^{-25} \pm 3.48149 \cdot 10^{-26}$
18.3	$2.37489 \cdot 10^{-25} \pm 1.80981 \cdot 10^{-26}$
18.4	$1.00788 \cdot 10^{-25} \pm 9.97127 \cdot 10^{-27}$
18.5	$4.53696 \cdot 10^{-26} \pm 4.9433 \cdot 10^{-27}$

Table 14: Unfolded flux, EPOS-LHC, primary H, SVD Unfolding.

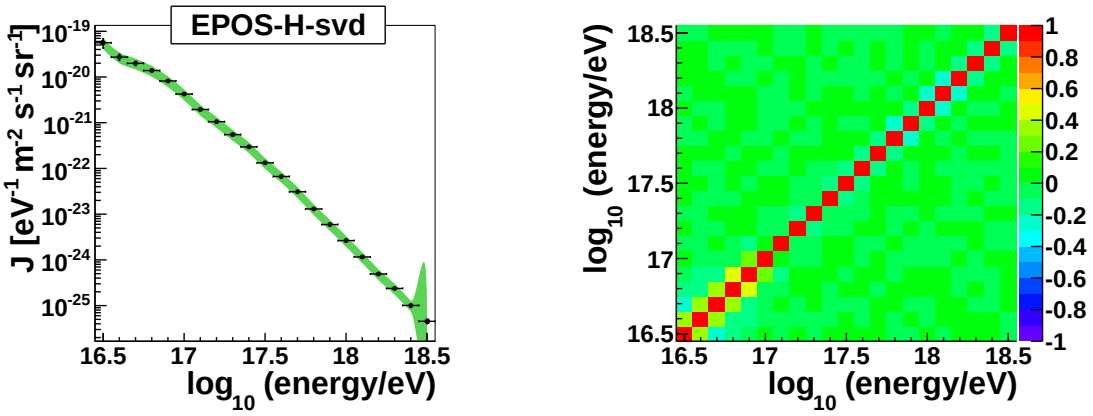

(a) Unfolded flux $J[eV^{-1}m^{-2}s^{-1}sr^{-1}]$. **(b)** Correlation matrix.

Figure 6.31: EPOS-LHC, H, SVD Unfolding

Energy in $log_{10}E/eV$	$J[eV^{-1}m^{-2}s^{-1}sr^{-1}]$
16.5	$5.2267 \cdot 10^{-20} \pm 8.43069 \cdot 10^{-21}$
16.6	$2.62298 \cdot 10^{-20} \pm 2.65854 \cdot 10^{-21}$
16.7	$1.82327 \cdot 10^{-20} \pm 1.29605 \cdot 10^{-21}$
16.8	$1.20981 \cdot 10^{-20} \pm 6.36524 \cdot 10^{-22}$
16.9	$7.44384 \cdot 10^{-21} \pm 3.06091 \cdot 10^{-22}$
17.0	$4.0742 \cdot 10^{-21} \pm 1.32448 \cdot 10^{-22}$
17.1	$2.48044 \cdot 10^{-21} \pm 7.17841 \cdot 10^{-23}$
17.2	$1.27421 \cdot 10^{-21} \pm 3.32105 \cdot 10^{-23}$
17.3	$6.92211 \cdot 10^{-22} \pm 1.70392 \cdot 10^{-23}$
17.4	$3.58854 \cdot 10^{-22} \pm 8.67688 \cdot 10^{-24}$
17.5	$1.59873 \cdot 10^{-22} \pm 3.92205 \cdot 10^{-24}$
17.6	$7.80546 \cdot 10^{-23} \pm 1.94639 \cdot 10^{-24}$
17.7	$3.63624 \cdot 10^{-23} \pm 9.56124 \cdot 10^{-25}$
17.8	$1.57536 \cdot 10^{-23} \pm 4.56352 \cdot 10^{-25}$
17.9	$6.57579 \cdot 10^{-24} \pm 2.08889 \cdot 10^{-25}$
18.0	$2.82258 \cdot 10^{-24} \pm 1.01559 \cdot 10^{-25}$
18.1	$1.18735 \cdot 10^{-24} \pm 4.9866 \cdot 10^{-26}$
18.2	$4.91252 \cdot 10^{-25} \pm 2.4402 \cdot 10^{-26}$
18.3	$2.3393 \cdot 10^{-25} \pm 1.33763 \cdot 10^{-26}$
18.4	$9.73091 \cdot 10^{-26} \pm 6.78716 \cdot 10^{-27}$
18.5	$4.76134 \cdot 10^{-26} \pm 4.06459 \cdot 10^{-27}$

Table 15: Unfolded flux, EPOS-LHC, primary Fe, Bayes Unfolding.

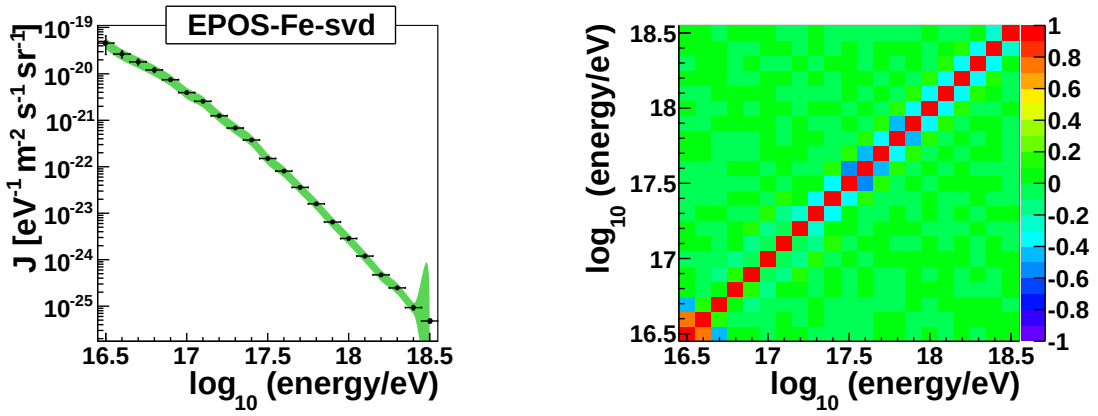

(a) Unfolded flux $J[eV^{-1}m^{-2}s^{-1}sr^{-1}]$. **(b)** Correlation matrix.

Figure 6.32: EPOS-LHC, Fe, SVD Unfolding

Energy in $log_{10}E/eV$	$J[eV^{-1}m^{-2}s^{-1}sr^{-1}]$
16.5	$4.584 \cdot 10^{-20} \pm 1.97725 \cdot 10^{-20}$
16.6	$2.66477 \cdot 10^{-20} \pm 4.56787 \cdot 10^{-21}$
16.7	$1.80834 \cdot 10^{-20} \pm 2.5418 \cdot 10^{-21}$
16.8	$1.20994 \cdot 10^{-20} \pm 1.39359 \cdot 10^{-21}$
16.9	$7.45776 \cdot 10^{-21} \pm 7.13505 \cdot 10^{-22}$
17.0	$3.93967 \cdot 10^{-21} \pm 3.60115 \cdot 10^{-22}$
17.1	$2.56215 \cdot 10^{-21} \pm 1.97788 \cdot 10^{-22}$
17.2	$1.25 \cdot 10^{-21} \pm 9.83418 \cdot 10^{-23}$
17.3	$6.81162 \cdot 10^{-22} \pm 5.0521 \cdot 10^{-23}$
17.4	$3.76319 \cdot 10^{-22} \pm 2.42567 \cdot 10^{-23}$
17.5	$1.50498 \cdot 10^{-22} \pm 1.10189 \cdot 10^{-23}$
17.6	$8.06081 \cdot 10^{-23} \pm 4.96863 \cdot 10^{-24}$
17.7	$3.59482 \cdot 10^{-23} \pm 2.09859 \cdot 10^{-24}$
17.8	$1.59065 \cdot 10^{-23} \pm 9.95769 \cdot 10^{-25}$
17.9	$6.46132 \cdot 10^{-24} \pm 4.03154 \cdot 10^{-25}$
18.0	$2.85388 \cdot 10^{-24} \pm 1.8633 \cdot 10^{-25}$
18.1	$1.19577 \cdot 10^{-24} \pm 8.3284 \cdot 10^{-26}$
18.2	$4.71405 \cdot 10^{-25} \pm 4.03485 \cdot 10^{-26}$
18.3	$2.47111 \cdot 10^{-25} \pm 2.1172 \cdot 10^{-26}$
18.4	$9.30644 \cdot 10^{-26} \pm 1.04692 \cdot 10^{-26}$
18.5	$4.79938 \cdot 10^{-26} \pm 4.96755 \cdot 10^{-27}$

Table 16: Unfolded flux, EPOS-LHC, primary Fe, SVDUnfolding.

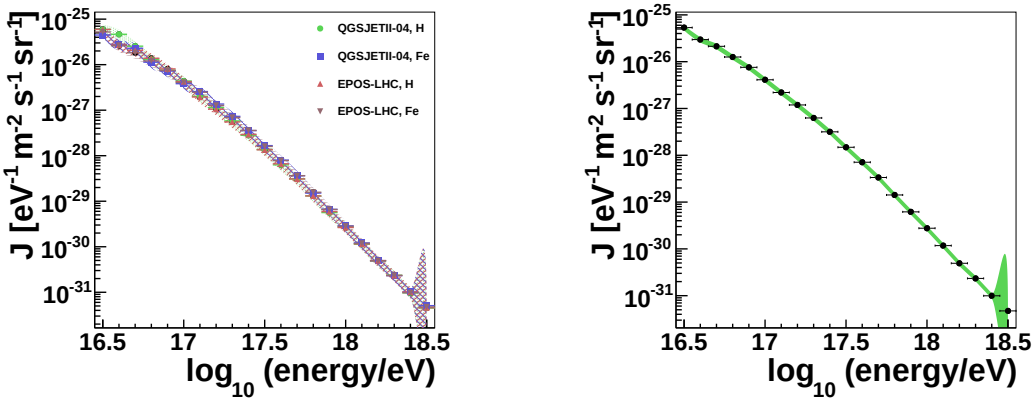

(a) All results for Bayes Unfolding. **(b)** Mean flux $J[eV^{-1}m^{-2}s^{-1}sr^{-1}]$.

Figure 6.33: Bayes Unfolding

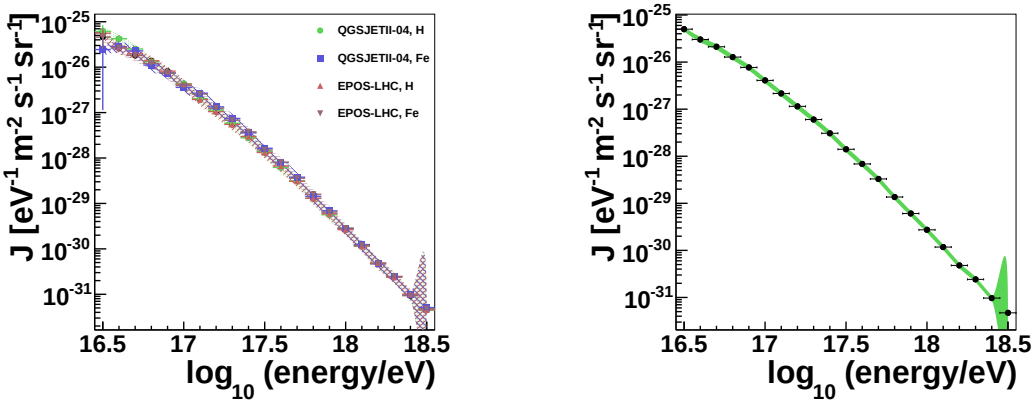

(a) All results for SVD Unfolding. **(b)** Mean flux $J[eV^{-1}m^{-2}s^{-1}sr^{-1}]$.

Figure 6.34: SVD Unfolding

In order to compare the results to the energy spectrum measured by other experiments, a weighted mean of all distributions corresponding to one unfolding algorithm is calculated. The result for Bayes Unfolding and SVD Unfolding are given in fig. 6.33b and 6.34b respectively.

7 Summary and Outlook

To be able to compare the results from different experiments with each other it is important to unfold the obtained data. Therefore two unfolding algorithms have been presented in this thesis. MC studies provided a tool to test the algorithms and find the optimum regularization parameters.
Furthermore the MC data enables an estimation for the systematic uncertainties of the unfolding process. Statistical errors have been obtained through full error propagation and are presented in correlation matrices.

Finally, the unfolding yield two distributions for the flux, measured by the HEAT telescopes at the Pierre Auger Observatory. Both algorithms give results that are well compatible with each other as well as with other experiments (see fig. 7.1).

All in all the unfolding of the energy spectrum and the reconstruction of the flux could be performed succesfully.

Outlook

First, the systematics in the lowest energy bins could be further investigated, as there appears to be some effects to the data. Furthermore, enhanced MC samples might be a good extension to the analysis. This includes more events for the given interaction

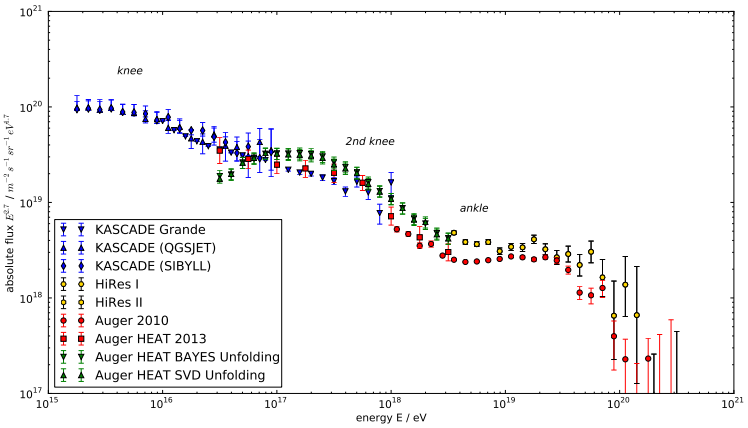

Figure 7.1: Absolute flux measured by multiple experiments. This work (green triangles) is in good agreement with the other results shown. Data from Kascade [40], HiRes [41], Auger [42] and Auger HEAT [25]. Script written by Tim Niggemann.

models and primary particles as well as other models.

Also, other unfolding algorithms could be studied and applied, like TRUEE [43, 44], which is a rework developed at the TU Dortmund of the RUN algorithm [45] introduced by V. Blobel.

References

Bibliography

[1] The Pierre Auger Collaboration, *The Pierre Auger Cosmic Ray Observatory*, ArXiv e-prints, arXiv: 1502.01323 (2015).

[2] M. Kleifges, *Extension of the Pierre Auger Observatory using high-elevation fluorescence telescopes (HEAT)*, in PROCEEDINGS OF THE 31st ICRC, LODZ (Pierre Auger Collaboration, 2009).

[3] T. Bergmann et al., *One-dimensional hybrid approach to extensive air shower simulation*, Astropart. Phys. **26**, 420–432, eprint: astro-ph/0606564 (2007).

[4] S. Argiro et al., *The Offline Software Framework of the Pierre Auger Observatory*, Nucl. Instrum. Meth. **A580**, 1485–1496, arXiv: 0707.1652 (2007).

[5] G. D'Agostini, *A multidimensional unfolding method based on Bayes' theorem*, Nuclear Instruments and Methods in Physics Research Section A: Accelerators, Spectrometers, Detectors and Associated Equipment **362**, 487–498 (1995).

[6] A. Höcker and V. Kartvelishvili, *SVD approach to data unfolding*, Nuclear Instruments and Methods in Physics Research Section A: Accelerators, Spectrometers, Detectors and Associated Equipment **372**, 469–481 (1996).

[7] V. F. Hess, *Beobachtungen der durchdringenden Strahlung bei sieben Freiballonfahrten*, Phys. Z. **13**, 1084 (1912).

[8] W. Bothe and W. Kolhörster, *Das Wesen der Höhenstrahlung*, German, Zeitschrift für Physik **56**, 751–777 (1929).

[9] P. Auger et al., *Extensive Cosmic-Ray Showers*, Rev. Mod. Phys. **11**, 288–291 (1939).

[10] R. Aloisio, V. Berezinsky, and A. Gazizov, *Transition from galactic to extragalactic cosmic rays*, Astropart. Phys. **39-40**, 129–143, arXiv: 1211.0494 (2012).

[11] J. Blümer, R. Engel, and J. R. Hörandel, *Cosmic rays from the knee to the highest energies*, Progress in Particle and Nuclear Physics **63**, 293–338, arXiv: 0904.0725 (2009).

[12] A. Haungs et al., *KCDC - The KASCADE Cosmic-ray Data Centre*, J. Phys. Conf. Ser. **632**, 012011, arXiv: 1504.06696 (2015).

[13] W. Heitler, *The Quantum Theory of Radiation*, Dover Books on Physics and Chemistry, Dover Publications () 1954.

[14] T. Gaisser and A. Hillas, eds., *in Proc. 15th Int. Cosmic Ray Conf.* (Plovdiv, Bulgaria), () 1977, p. 358.

[15] K. Greisen, ed., *in Prog. of Cosmic Ray Phys.* (North-Holland Publ. Co., Amsterdam), () 1956, p. 1.

[16] J. N. K. Kamata, ed., *Prog. Tboer. Phys.* (Kyoto), () 1958, p. 93.

[17] The Pierre Auger Collaboration Pierre Auger, *The Pierre Auger Observatory: Contributions to the 33rd International Cosmic Ray Conference (ICRC 2013)*, arXiv: 1307.5059 (2013).

[18] I. Allekotte et al. Pierre Auger, *The Surface Detector System of the Pierre Auger Observatory*, Nucl.Instrum.Meth. **A586**, 409–420, arXiv: 0712.2832 (2008).

[19] The Pierre Auger Collaboration, *The Fluorescence Detector of the Pierre Auger Observatory*, ArXiv e-prints, arXiv: 0907.4282 (2009).

[20] P. e. a. Abreu Pierre Auger, *Antennas for the detection of radio emission pulses from cosmic-ray induced air showers at the Pierre Auger Observatory*, Journal of Instrumentation **7**, 11P, arXiv: 1209.3840 (2012).

[21] H. Klages and Pierre Auger Collaboration, *Enhancements to the Southern Pierre Auger Observatory*, Journal of Physics Conference Series **375**, 052006, 052006, arXiv: 1107.4807 (2012).

[22] P. Abreu et al. Pierre Auger, *The Pierre Auger Observatory V: Enhancements*, in Proceedings, 32nd International Cosmic Ray Conference (ICRC 2011) (2011), arXiv: 1107.4807.

[23] V. Olmos Gilbaja, *A complete method to obtain the energy spectrum of inclined cosmic rays detected with the Pierre Auger Observatory*, GAP2013-037 (2013).

[24] F. Arqueros, J. R. Hörandel, and B. Keilhauer, *Air fluorescence relevant for cosmic-ray detection - Summary of the 5th fluorescence workshop, El Escorial 2007*, Nuclear Instruments and Methods in Physics Research A **597**, 1–22, arXiv: 0807.3760 (2008).

[25] N. Scharf, *The energy spectrum of cosmic rays measured with the HEAT extension at the Pierre Auger Observatory*, GAP: 2014-068 (2013).

[26] J. C. de No, *Monitoring of camera positions for Auger Fluorescence Telescopes.*

[27] T. Pierog et al., *First Results of Fast One-dimensional Hybrid Simulation of EAS Using CONEX*, Nucl. Phys. Proc. Suppl. **151**, 159–162, eprint: astro-ph/0411260 (2006).

[28] D. Heck et al., *CORSIKA: A Monte Carlo code to simulate extensive air showers* (1998).

[29] S. Ostapchenko, *QGSJET-II: physics, recent improvements, and results for air showers*, EPJ Web Conf. **52**, 02001 (2013).

[30] T. Pierog et al., *EPOS LHC: Test of collective hadronization with data measured at the CERN Large Hadron Collider*, Phys. Rev. **C92**, 034906, arXiv: 1306.0121 (2015).

[31] S. J. Sciutto, *Air shower simulations with the aires system*, in Proceedings, 26th International Cosmic Ray Conference, August 17-25, 1999, Salt Lake City, [1,411(1999)] (1999), p. 411, arXiv: astro-ph/9905185.

[32] I. Maris, *Utilities for ADST-Analysis*, GAP: 2009-012 (2009).

[33] G. D'Agostini, *Improved iterative Bayesian unfolding*, arXiv: 1010.0632.

[34] C. Lawson and R. Hanson, *Solving Least Squares Problems*, Society for Industrial and Applied Mathematics () 1995, pp. 188–192, eprint: http://epubs.siam.org/doi/pdf/10.1137/1.9781611971217.

[35] N. D. Gagunashvili, *Chi-square tests for comparing weighted histograms*, Nuclear Instruments and Methods in Physics Research A **614**, 287–296, arXiv: 0905.4221 (2010).

[36] R. Doe, *Kolmogorov-Smirnov Goodness-of-Fit Test*, (Dec. 2015) http://www.itl.nist.gov/div898/handbook/eda/section3/eda35g.htm.

[37] K. Pearson, *On the theory of contingency and its relation to association and normal correlation*, Cambridge University Press (London) 1904, 35 S.

[38] C. D. Giulio, *Energy calibration of data recorded with the surface detectors of the Pierre Auger Observatory*, in PROCEEDINGS OF THE 31st ICRC, LODZ (Pierre Auger Collaboration, 2009).

[39] P. Abreu et al., *The exposure of the hybrid detector of the Pierre Auger Observatory*, Astroparticle Physics **34**, 368–381, arXiv: 1010.6162 (2011).

[40] T. Antoni et al. KASCADE, *KASCADE measurements of energy spectra for elemental groups of cosmic rays: Results and open problems*, Astropart. Phys. **24**, 1–25, arXiv: astro-ph/0505413 (2005).

[41] R. U. Abbasi et al. High Resolution Flys Eye Collaboration, *First Observation of the Greisen-Zatsepin-Kuzmin Suppression*, Phys. Rev. Lett. **100**, 101101 (2008).

[42] J. Abraham et al., *Measurement of the energy spectrum of cosmic rays above 10^{18} eV using the Pierre Auger Observatory*, Physics Letters B **685**, 239–246, arXiv: 1002.1975 (2010).

[43] N. Milke, *TRUEE Manual*, 2.5, (http://app.tu-dortmund.de/TRUEE/) 2012.

[44] N. Milke et al., *Solving inverse problems with the unfolding program TRUEE: Examples in astroparticle physics*, Nuclear Instruments and Methods in Physics Research A **697**, 133–147, arXiv: 1209.3218 (2013).

[45] V. Blobel, *An Unfolding method for high-energy physics experiments*, in Advanced statistical techniques in particle physics. Proceedings, Conference, Durham, UK, March 18-22, 2002 (2002), pp. 258–267, arXiv: hep-ex/0208022.

Appendices

A Offline Modul Sequence

ModulSequence.xml file used in the Offline framework to simulate and reconstruct air showers.

```
<sequenceFile>

  <enableTiming/>

  <moduleControl>

<!-- SIMULATION -->
   <loop numTimes="unbounded" pushEventToStack="yes">

      <module> EventFileReaderOG </module>
      <module> MCShowerCheckerOG </module>

<loop numTimes="1" pushEventToStack="yes">
  <module> EventGeneratorOG </module>
<!-- FD simulation part -->
<try>  <!-- catch triggerless events for RecData* -->
<module> FdSimEventCheckerOG  </module>
<module> ShowerLightSimulatorKG  </module>
<module> LightAtDiaphragmSimulatorKG  </module>
<module> ShowerPhotonGeneratorOG  </module>
<module> TelescopeSimulatorKG  </module>
<module> FdBackgroundSimulatorOG  </module>
<module> FdElectronicsSimulatorOG  </module>
<module> FdTriggerSimulatorOG  </module>
</try>
<try>
<module> SdSimpleSimKG </module>
</try>
<try>  <!-- catch triggerless events for RecData* -->
<!-- Trigger and Event builder -->
<module> CentralTriggerSimulatorXb  </module>
<module> CentralTriggerEventBuilderOG  </module>
<module> EventBuilderOG  </module>
</try> <!-- catch trigger Continues -->
</loop>
```

```
  <!-- RECONSTRUCTION -->

<loop numTimes="1" pushEventToStack="yes">

<module> EventCheckerOG </module>

<try>

  <!-- Hybrid reconstruction -->
<module> FdCalibratorOG           </module>
  <module> FdEyeMergerKG            </module> <!-- COHE -->
<module> FdPulseFinderOG          </module>
<module> FdSDPFinderOG            </module>
<module> FdAxisFinderOG           </module>
<module> HybridGeometryFinderOG   </module>
<module> HybridGeometryFinderWG   </module> <!-- COHE -->
<module> FdApertureLightKG        </module> <!-- COHE -->
<module> FdEnergyDepositFinderKG  </module> <!-- COHE -->
</try>
       <!-- export the ADST -->
       <module> RecDataWriterNG </module>
</loop>
   </loop>

</moduleControl>

</sequenceFile>
```

B Cut steering file

These are the cuts applied to all MC and data events. For a description see section 4.3 and [32]. The list is equal to this of [25] and the same cuts are applied, as the data acquired there was used in this analysis too.

```
hasEnergy              #  bolean cut:succesfull energy reconstruction
isHybrid               #  bolean cut:Event is a hybrid event
eyeCut 100000          #  Only eye 6 (COHE) allowed
maxZenithFD 60.        #  maximum zenith angle
maxCoreTankDist 800.   #  maximum distance core-hybrid-tank in m
energyError 0.2        #  max error on energy (relative)
maxDirCFrac 50.        #  max direct Cherenkov fraction in %
xMaxInFOV 20.0         #  max distance of xMax to borders
profileChi2 2.5        #  max reduced GH chi2
maxDepthHole 30.       #  maximum hole in profile in %
skipSaturated          #  bolean cut:Events with saturated pixels removed
!badPixels 1           #  bolean cut:Events with bad pixels removed
```

C Acknowledgement

I would like to thank everyone, who helped me during this master thesis. My family for all the support and warm words, whenever i needed some. Anna, for always being there and supporting me in any given way. Furthermore i want to emphasize my thankfulness to Prof. Dr. Hebbeker, for offering this interesting and complex topic as a master thesis to me.
Thanks to Matthias Plum, for being a helpful tutor, getting me started and always being a nice office co-worker.
Also to Nils Scharf, for providing a basement for my thesis with his dissertation.
The whole Auger group, and especially the Aachen part (III A and B) deserves a thank you, too, for good conversations and meeting.

D Affidavit

Hiermit erkläre ich, Sebastian Hartmann, dass ich die vorgelegte Masterarbeit selbständig verfasst und – einschließlich eventuell beigefügter Abbildungen und Skizzen – keine anderen als die im Literaturverzeichnis angegebenen Quellen, Darstellungen und Hilfsmittel benutzt habe. Dies gilt in gleicher Weise für gedruckte Quellen wie für Quellen aus dem Internet.

Ich habe alle Passagen und Sätze der Arbeit, die dem Wortlaut oder dem Sinne nach anderen Werken entnommen sind, in jedem einzelnen Fall deutlich als Entlehnung gekennzeichnet. Außerdem erkläre ich, dass die vorgelegte Arbeit zuvor weder von mir noch von einer anderen Person an dieser oder einer anderen Universität eingereicht wurde.